

A Census of the Extended Neutral Hydrogen around 18 MHONGOOSE Galaxies

Amy Sardone^{1,2}, D. J. Pisano^{3,4,5}, N. M. Pingel^{3,4,6}, A. Sorgho⁷, Claude Carignan^{7,8}, and W. J. G. de Blok^{7,9,10} Department of Astronomy, The Ohio State University, 140 West 18th Avenue, Columbus, OH 43210, USA; sardone.4@osu.edu

Center for Cosmology and Astroparticle Physics, 191 West Woodruff Avenue, Columbus, OH 43210, USA

Department of Physics and Astronomy, West Virginia University, Morgantown, WV 26506, USA

Gravitational Waye and Cosmology Center, Chestnut Ridge Research Building, Morgantown, WV 26505 USA

Adjunct Astronomer at Green Bank Observatory, Green Bank, WV 24944

Research School of Astronomy & Astrophysics, Australian National University, Canberra, ACT 2611, Australia

Department of Astronomy, University of Cape Town, Private Bag X3, Rondebosch 7701, South Africa

Laboratoire de Physique et de Chimie de l'Environnement, Observatoire d'Astrophysique de l'Université Ouaga I Pr Joseph Ki-Zerbo (ODAUO), 03 BP 7021, Ouaga 03, Burkina Faso

Netherlands Institute for Radio Astronomy (ASTRON), Oude Hoogeveensedijk 4, 7991 PD Dwingeloo, The Netherlands ¹⁰ Kapteyn Astronomical Institute, University of Groningen, PO Box 800, 9700 AV Groningen, The Netherlands Received 2020 July 10; revised 2021 January 14; accepted 2021 January 19; published 2021 March 26

Abstract

We present the analysis of the diffuse, low column density H1environment of 18 MHONGOOSE galaxies. We obtained deep observations with the Robert C. Byrd Green Bank Telescope and reached down to a 3σ column density detection limit of $N_{\rm HI}=6.3\times10^{17}\,{\rm cm^{-2}}$ over a 20 km s⁻¹ line width. We analyze the environment around these galaxies, with a focus on H1gas that reaches column densities below $N_{\rm HI}=10^{19}\,{\rm cm^{-2}}$. We calculate the total amount of H1gas in and around the galaxies, revealing that nearly all of these galaxies contained excess H1outside of their disks. We quantify the amount of diffuse gas in the maps of each galaxy, defined by H1gas with column densities below $10^{19}\,{\rm cm^{-2}}$, and find a large spread in percentages of diffuse gas. However, by binning the percentage of diffuse H1into quarters, we find that the bin with the largest number of galaxies is the lowest quartile (0%-25% diffuse H1). We identified several galaxies that may be undergoing gas accretion onto the galaxy disk using multiple methods of analysis, including azimuthally averaging column densities beyond the disk, and identifying structure within our integrated intensity (moment 0) maps. We measured H1 mass outside the disks of most of our galaxies, with rising cumulative flux even at large radii. We also find a strong correlation between the fraction of diffuse gas in a galaxy and its baryonic mass, and we test this correlation using both Spearman and Pearson correlation coefficients. We see evidence of a dark matter halo mass threshold of $M_{\rm halo} \sim 10^{11.1}\,M_{\odot}$ in which galaxies with high fractions of diffuse H1all reside below. It is in this regime that cold-mode accretion should dominate. Finally, we suggest a rotation velocity of $v_{\rm rot} \sim 80\,{\rm km\,s^{-1}}$ as an upper threshold to find diffuse-gas-dominated galaxies.

Unified Astronomy Thesaurus concepts: Circumgalactic medium (1879); Extragalactic astronomy (506); Galaxy evolution (594); Galaxy accretion (575); Galaxy structure (622)

1. Introduction

The question of how galaxies get their gas and how they use this gas to continue to form stars remains among the main unanswered questions in astronomy. We know that as the star formation rate (SFR) density over cosmic time has decreased since a redshift of $z \sim 2$ (Madau & Dickinson 2014), the neutral hydrogen gas density has remained nearly constant since $z \sim 4$ (Rhee et al. 2018). Di Teodoro & Fraternali (2014) show that mergers of dwarf galaxies with spiral galaxies do not provide sufficient extra mass to sustain star formation in those galaxies. Even so, if star formation in spiral galaxies is not sustained by mergers alone, then they must be accreting the gas from the intergalactic medium (IGM).

Gas accreting from the IGM flows into the galaxy via diffuse filamentary structures (Birnboim & Dekel 2003; Katz et al. 2003; Kereš et al. 2005). The gas travels from the cosmic web (Bond et al. 1996) through these filaments and into the circumgalactic medium (CGM) of galaxies before falling onto the galaxy disk. The process of accretion described here typically proceeds via the hot or the cold mode (Kereš et al. 2005), where gas entering the halo either becomes shock heated to the virial temperature before cooling and condensing onto the galaxy disk or flows along cold filaments through the CGM

and remains cool as it falls onto the disk. While gas in both scenarios is predominantly ionized, the gas accreting via the cold mode maintains a small neutral fraction, making detection feasible. Cold accretion dominates in the lower-mass galaxy regime and favors low galaxy density environments. Observations of the CGM and disks of galaxies encompassing a range of these parameters will provide insight into cold accretion from the IGM and potentially direct detections of this gas falling onto galaxies.

Deep H I surveys provide the observational link to direct detections of the effects of cold-mode accretion from the IGM. The MeerKAT H I Observations of Nearby Galactic Objects; Observing Southern Emitters (MHONGOOSE; 11 de Blok et al. 2016) survey will provide high spatial resolution, high column density sensitivity maps of 30 nearby disk and dwarf galaxies. Most other H I surveys achieve one or the other, but not both, with the exception of the IMAGINE 12 survey with ATCA, which still has a much lower angular resolution than MHONGOOSE. HIPASS (Koribalski et al. 2004) and ALFALFA (Haynes et al. 2011) surveys provide an extremely large number of H I detections, although neither at high

¹¹ https://mhongoose.astron.nl

¹² http://www.w3.org/1999/xlink

Table 1
Sample of MHONGOOSE Galaxies

Source	R.A.(J2000) (h:m:s)	Decl.(J2000) (°:':")	D (Mpc)	incl. (deg)	D ₂₅ (arcmin)	$\frac{\log_{10} M_{\star}}{(M_{\odot})}$
(1)	(2)	(3)	(4)	(5)	(6)	(7)
ESO 300-G014	03:09:37	-41:01:50	12.9	61.2	4.47	8.72
ESO 300-G016	03:10:10	-40:00:11	9.3	35.6	0.78	
ESO 302-G014	03:51:40	-38:27:08	11.7	27.6	1.35	7.79
ESO 357-G007	03:10:24	-33:09:22	17.8	72.0	1.29	8.31
KK 98-195	13:21:08	-31:31:45	5.2	55.7	0.45	
KKS 2000-23	11:06:12	-14:24:26	12.7	90.0	0.6	
NGC 1371	03:35:01	-24:56:00	20.4	47.5	4.9	10.7
NGC 1592	04:29:40	-27:24:31	13.0	64.4	1.02	8.13
NGC 1744	04:59:57	-26:01:20	10.0	69.9	5.25	9.19
NGC 3511	11:03:23	-23:05:12	14.2	72.6	6.03	9.63
NGC 5068	13:18:54	-21:02:21	6.9	30.1	7.41	9.32
NGC 5170	13:29:48	-17:57:59	28.0	90.0	7.94	10.72
NGC 5253	13:39:55	-31:38:24	3.0	70.1	5.01	8.57
NGC 7424	22:57:18	-41:04:14	13.5	32.4	5.01	9.31
UGCA 015	00:49:49	-21:00:54	3.3	67.4	1.62	6.74
UGCA 250	11:53:24	-28:33:11	24.4	90.0	3.63	9.74
UGCA 307	12:53:57	-12:06:21	8.6	62.0	1.82	7.96
UGCA 320	13:03:16	-17:25:23	7.7	90.0	6.76	8.11

Note. Positions listed in Columns (2)–(3) and distances in Column (4) are gathered from NED. Inclination angles from face-on in Column (5) and the optical diameter, D_{25} , measured at the 25th mag arcsec⁻² isophote in the *B*-band values are taken from HyperLEDA: http://leda.univ-lyon1.fr. Stellar masses were obtained from Leroy et al. (2019).

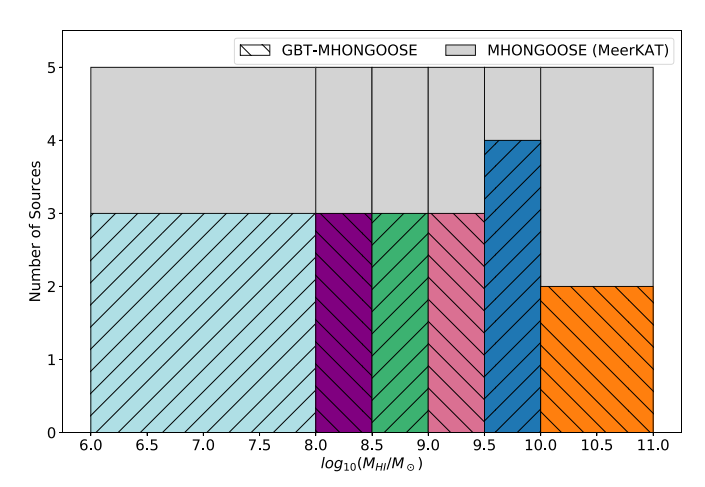


Figure 1. Histogram of H I masses in the MHONGOOSE sample. Each bin is separated by color and hatch marking. The hatch markings (both directions) identify the GBT-MHONGOOSE sample, and the gray filled region represents the full MHONGOOSE with MeerKAT sample. This histogram demonstrates the coverage of the H I mass range in both MHONGOOSE samples. Note that the lowest and highest mass bins are larger owing to the scarcity of galaxies meeting the survey criteria in those mass ranges.

resolution nor with column density sensitivities matching ours. High-resolution surveys such as THINGS (Walter et al. 2008) and HALOGAS (Heald et al. 2011; one of the first high-resolution surveys designed to systematically detect accretion of H I) achieve column density sensitivities of $\sim\!10^{20}$ and $\sim\!10^{19}$ cm $^{-2}$, respectively. These levels of column densities enable detection of clumpy H I that could be missed by a single-dish telescope, yet they would not be low enough to detect any extended or more diffuse gas accreting from the IGM. The MHONGOOSE survey will use the South African MeerKAT radio telescope, a 64-dish precursor to the Square Kilometre Array (SKA), to map these 30 galaxies to a 3σ column density detection limit of 7.5×10^{18} cm $^{-2}$ over a

 $16\,\mathrm{km\,s}^{-1}$ line width at an angular resolution of 30". At their poorest angular resolution, 90", this column density limit goes down to $5.5 \times 10^{17}\,\mathrm{cm}^{-2}$. The high-resolution maps produced by MHONGOOSE will further our understanding of how galaxies get their gas, how galaxies sustain star formation, and how matter that we can detect relates to the dark matter associated with galaxies, influencing galactic evolution. Specifically, this survey will help us to understand how gas flows in or out of galaxies, the conditions that allow the fueling of star formation, accretion from the IGM, and ultimately its connection to the cosmic web (e.g., Carignan 2016). The first of these data are presented in de Blok et al. (2020), detailing their detection of low column density H I clouds and a filament extending off of ESO 302-G014, which could be the result of a minor interaction with a dwarf galaxy.

Early observations of a subset of MHONGOOSE galaxies were presented in (Sorgho et al. 2019, hereafter S19), using MeerKAT, KAT-7, the seven-dish MeerKAT precursor array, and the Robert C. Byrd Green Bank Telescope (GBT). The subset of galaxies mapped with the GBT are presented here, with the description of the MHONGOOSE sample in Section 2. We describe our GBT observations and data reduction process in Section 3. Two galaxies not presented in S19, NGC 1744 and NGC 7424, are presented in Section 4. The analysis we performed on all of these galaxies is described in Section 5. Our results are presented in Section 6. We discuss these results in Section 7 and summarize our findings in Section 8.

2. MHONGOOSE Galaxy Sample

The MHONGOOSE sample of galaxies was chosen from galaxies having been previously detected in multiple wavelengths (H I from HIPASS, $H\alpha$, optical, infrared, and ultraviolet from the SINGG and SUNGG surveys; Meurer et al. 2006). MHONGOOSE galaxies were primarily selected to cover a large range of H I masses. A secondary parameter used in the

Table 2
H I Measurements and Derived Properties of MHONGOOSE Galaxies

Source (1)	$\sigma_{\rm rms}$ (mJy) (2)	$S_{\rm H\ I}$ (Jy km s ⁻¹) (3)	$V_{\rm sys}$ (km s ⁻¹) (4)	W_{50} (km s ⁻¹) (5)	W_{20} (km s ⁻¹) (6)	$log_{10}N_{HI\ 1\sigma}$ (cm^{-2}) (7)	$log_{10}N_{HI\ 3\sigma}$ (cm^{-2}) (8)	$ \log_{10} M_{1\sigma} \\ (M_{\odot}) \\ (9) $	$\log_{10} M_{H i} \atop (M_{\odot}) \atop (10)$	$\log_{10} M_{\rm dyn}$ (M_{\odot}) (11)	f _{H I} (12)
ESO 300-G014	10.4	33.6	955.0	129.2	145.2	17.35	18.33	6.42	9.12	10.36	0.058
ESO 300-G016	9.1	4.9	710.5	30.1	43.9	17.29	18.27	6.07	8.0	8.78	0.167
ESO 302-G014	9.6	13.7	869.3	65.5	87.1	17.31	18.29	6.29	8.65	9.91	0.055
ESO 357-G007	4.9	15.0	1118.3	118.4	148.5	17.02	18.0	6.37	9.05	9.91	0.137
KK 98-195	5.9	8.1	570.6	27.1	42.2	17.1	18.08	5.38	7.71	7.95	0.577
KKS 2000-23	5.3	14.2	1037.5	80.2	96.8	17.06	18.03	6.11	8.73	9.02	0.515
NGC 1371	7.6	90.9	1454.3	386.4	403.8	17.21	18.19	6.68	9.95	11.63	0.021
NGC 1592	4.8	5.8	942.9	55.1	96.2	17.01	17.99	6.08	8.36	9.34	0.104
NGC 1744	3.2	174.7	743.4	191.1	207.2	16.75	17.82	5.59	9.62	10.56	0.112
NGC 3511	8.3	74.6	1130.8	272.4	308.7	17.25	18.23	6.4	9.55	11.11	0.028
NGC 5068	4.8	191.5	667.7	67.9	108.0	17.01	17.99	5.53	9.33	10.53	0.063
NGC 5170	6.2	106.2	1546.7	504.0	523.0	17.13	18.1	6.87	10.29	11.94	0.023
NGC 5253	8.3	57.6	404.5	63.4	99.1	17.25	18.23	5.05	8.09	9.38	0.051
NGC 7424	5.6	297.2	934.9	152.6	170.5	16.99	18.06	6.1	10.11	10.99	0.13
UGCA 015	5.2	5.2	293.6	25.5	43.2	17.05	18.02	4.93	7.12	8.23	0.078
UGCA 250	7.6	87.6	1700.6	272.2	289.5	17.21	18.19	6.83	10.09	11.03	0.115
UGCA 307	5.0	32.0	822.9	68.5	95.2	17.03	18.01	5.74	8.75	9.42	0.211
UGCA 320	7.8	133.9	749.1	106.3	126.9	17.23	18.2	5.84	9.27	10.08	0.156

Note. Column (1): source name. Column (2): measured rms noise. Column (3): total integrated flux. Column (4): systemic velocity. Column (5): line width at 50% maximum. Column (6): line width at 20% maximum. Column (7): $1\sigma_{rms}$ column density sensitivity per channel. Column (8): $3\sigma_{rms}$ column density level over a 20 km s⁻¹ line width. Column (9): H I mass sensitivity. Column (10): H I mass. Column (11): dynamical mass. Column (12): neutral gas fraction.

selection, the SFR), enables the separation of H I coincident with the star-forming disk from extraplanar HI (e.g., Marasco et al. 2019). An equal number of galaxies were selected for each of six mass bins within a range of $6 < \log_{10}(M_{\rm HI}) < 11 M_{\odot}$ for a total of 30 galaxies with edge-on, face-on, and intermediate inclinations and a wide range of morphologies from dwarf irregulars to grand-design spirals. The sample of galaxies chosen for this set of observations coincides with the galaxies from the MHONGOOSE sample ($\delta < 10^{\circ}$), which can be seen by the GBT, which has a lower limit of declinations $\delta > -46^{\circ}$. This narrows the sample to 18 galaxies. Our GBT-MHONGOOSE sample sacrifices some of the uniformity of the original sample, while continuing to span the full range in HI masses. These galaxies similarly span a wide range of stellar masses (Table 1) falling between 6.7 $< \log_{10}(M_{\star}) < 10.7 M_{\odot}$ (Leroy et al. 2019). GBT integrated intensity (moment 0) maps and global HI profiles for 16 of these sources were presented in \$19, with two others, NGC 1744 and NGC 7424, having been observed separately and introduced here.

Each galaxy in the sample presented here, as well as the full MHONGOOSE sample, has a Galactic latitude of $|b| > 30^{\circ}$; peak H I fluxes, as detected in HIPASS, of greater than 50 mJy; and Galactic standard of rest velocities $> 200 \, \mathrm{km \, s^{-1}}$. Additionally, each source is below a decl. of $\delta < 10^{\circ}$ and is within a distance of 30 Mpc. The MHONGOOSE sample was chosen to uniformly cover the range of M_{HI} listed above, and our GBT sample covers that range nearly uniformly as well. Coverage of the H I mass range in each bin can be seen in Figure 1. We note that both the lowest and highest H I mass bins cover a larger mass range than the others owing to the scarcity of galaxies in those mass ranges that also meet the survey criteria. Further details on the MHONGOOSE sample selection can be found in de Blok et al. (2016).

3. Observations and Data Reduction

Observations for the 16 galaxies presented in S19 were carried out between 2016 August and 2017 January for project GBT16B-212. Each of these galaxies was observed for 10 hr each, for a total of 160 hr, with a theoretical brightness temperature noise sensitivity of $\sim 13 \,\mathrm{mK}$ over $5.2 \,\mathrm{km \, s^{-1}}$ channels. This noise sensitivity corresponds to a column density sensitivity of $N_{\rm HI} \sim 10^{18}\,{\rm cm}^{-2}$ over the same channel width. The two additional galaxies presented here (NGC 1744 and NGC 7424) were observed over the course of three GBT observing semesters (GBT15B-346, GBT16B-408, and GBT17A-478) from 2015 to 2017, for a total of 20 hr on NGC 1744 and 14 hr on NGC 7424. We observed these two galaxies over a bandwidth of 23.4 MHz, with a frequency resolution of 0.715 kHz. We used the sources 3C 48 and 3C 147, which have stable, well-understood fluxes, over the course of 12 observing nights to calibrate our data. We smoothed the data using a boxcar function with a final smoothed velocity resolution of 5.1 km s^{-1} , or 24.3 kHz. The remainder of the data reduction followed the same approach presented in \$19.

For each of our 18 galaxies, we used the GBT's VErsatile GBT Astronomical Spectrometer (VEGAS) back end in L band (1.15–1.73 GHz), where the FWHM beamwidth is 9.1, to map $2^{\circ} \times 2^{\circ}$ regions around each source. Data cubes were made for all 18 sources with pixel sizes of 1.75. The 16 sources from S19 were smoothed to a velocity resolution of 6.4 km s⁻¹.

We reached rms noise levels of 6-20 mK (3.2–10.4 mJy) in the cubes, corresponding to a 1σ column density sensitivity of $N_{\rm HI}=1.02\times10^{17}$ cm⁻² per 5.1 km s⁻¹ channel. At the noise level reached in this cube, a detectable signal at the 5σ level over a 20 km s⁻¹ line width is $N_{\rm HI}=2\times10^{18}$ cm⁻². Our 1σ mass sensitivities extend down to 1.6×10^5 M_{\odot} .

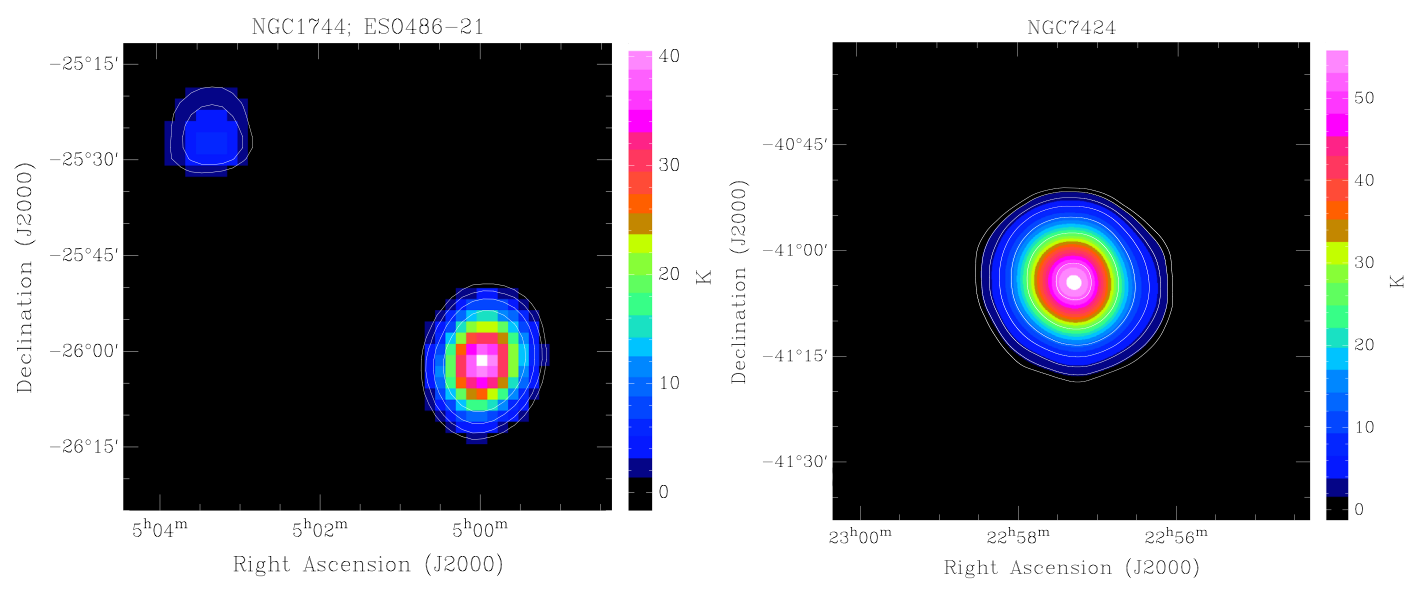


Figure 2. Left: integrated intensity (moment 0) map of NGC 1744 with companion ESO 486-G021 in the upper left corner. Contours are at 10, 20, and 40 times the integrated rms noise of 0.15 K. The column density equivalent to these contour levels is $N_{\rm HI}=0.69,\ 1.3,\ 2.7,\ {\rm and}\ 5.5\times10^{19}\ {\rm cm}^{-2}$. Right: integrated intensity (moment 0) map of NGC 7424. Contours are at 5, 10, 20, 40, 80, and 160 times the integrated rms noise of 0.16 K. The column density equivalent to these contour levels is $N_{\rm HI}=0.7,\ 1.48,\ 2.9,\ 5.9,\ {\rm and}\ 11.9\times10^{19}\ {\rm cm}^{-2}.$

4. Properties of Galaxies

Data cubes and integrated intensity (moment 0) maps for the 16 sources mentioned above were inspected and searched for anomalous H I in S19. In this section we will present the two additional sources, NGC 1744 and NGC 7424, and discuss their properties. These properties are listed in Table 2.

4.1. NGC 1744

NGC 1744 is an inclined (69°.9) SBcd¹³ galaxy. It is one of the more massive galaxies in our sample, for which we measured the total H I mass to be $7.6 \times 10^9 \, M_\odot$ ($\pm 2.1 \times 10^8$). We measured a total integrated flux of 174.7 Jy km s⁻¹ with an rms noise of $\sigma_{\rm rms} = 3.2$ mJy. We measured the full width at 20% maximum of the velocity profile to be 207.2 km s⁻¹ with a systemic velocity of 743 km s⁻¹, which we used to calculate a dynamical mass (see Section 5.2, Equation (4)) of NGC 1744 of $3.6 \times 10^{10} \, M_\odot$. These and other properties of NGC 1744 were tabulated in Table 2 and discussed further in Section 5.

We detected one additional source in the NGC 1744 data cube. Sbc (see footnote 11) galaxy ESO 486-G021 (Figure 3) is detected with an integrated H I flux density of 24.5 Jy km s $^{-1}$. The systemic velocities measured from the two galaxies differ by $\sim\!100\,\mathrm{km\,s^{-1}}$, and while this is low enough to investigate a potential interaction, we find their physical separation to be too great to make this likely. The angular separation is 58′, and at a distance of 12 Mpc, that becomes a physical separation of $\sim\!200\,\mathrm{kpc}$. We calculated the Jacobi radius, the maximum radius expected of a central galaxy and companion galaxy system, with

$$r_{\rm J} = R_{\rm Sep} \left(\frac{M_{\rm Comp}}{3M_{\rm Central}} \right)^{1/3}. \tag{1}$$

Here R_{Sep} is the physical separation between the centers of the two galaxies, M_{Comp} is the dynamical mass of the companion

galaxy, and $M_{\rm Central}$ is the dynamical mass of the central galaxy. This gives us a maximum expected radius of \sim 79 kpc using the dynamical mass, derived from the H I rotation velocity, of the companion of $2.2 \times 10^9 \, M_{\odot}$. It is evident that the 200 kpc projected separation is too large to consider a plausible interaction. Further, we do not detect any extraplanar or anomalous H I around NGC 1744 at these levels. A total H I intensity map including both NGC 1744 and ESO 486-G021 can be seen in Figure 2. Spectra of NGC 1744 can be seen in Figure 3. At a mass sensitivity in this cube of $7.2 \times 10^5 \, M_{\odot}$, and because we did not detect any anomalous H I, we can say that apart from ESO 486-G021 there are no additional sources with 3σ H I mass greater than $7.2 \times 10^5 \, M_{\odot}$.

4.2. NGC 7424

NGC 7424 is a mostly face-on SABcd galaxy (de Vaucouleurs et al. 1991), and one of the most HI massive sources in the survey. It falls into the mass bin $10 < \log_{10}(M_{\rm HI}) < 11~M_{\odot}$, one of the more unexplored mass regimes in low column density HI studies. We measured a total HI mass of $2.4 \times 10^{10}~M_{\odot}~(\pm 6.2 \times 10^8)$ in NGC 7424, where the mass sensitivity in the cube is $2.3 \times 10^6~M_{\odot}$, corresponding to a 1σ column density sensitivity of $N_{\rm HI} = 9.7 \times 10^{16}~{\rm cm}^{-2}~{\rm per}~5.1~{\rm km~s}^{-1}$ channel. NGC 7424's global HI profile and moment map can be seen in Figure 3.

We detected two additional galaxies within our map of NGC 7424: the Sd galaxy ESO 346-G018 with an angular separation of 58′, and the SBbc galaxy NGC 7462 with an angular separation from NGC 7424 of 64′. However, due to their positions at the edges of our cube, we cannot confidently measure the total H I. Instead, we can provide the following lower limits. We measured an integrated flux of 8.8 Jy km s⁻¹ for ESO 346-G018, with a line width at 20% maximum of 176 km s⁻¹ around a systemic velocity of 1875 km s⁻¹. NGC 7462 has an integrated flux lower limit of 25.0 Jy km s⁻¹, a 20% maximum line width of 205 km s⁻¹, and a systemic velocity of 1066 km s⁻¹. The total integrated profiles were

¹³ http://leda.univ-lyon1.fr

2000

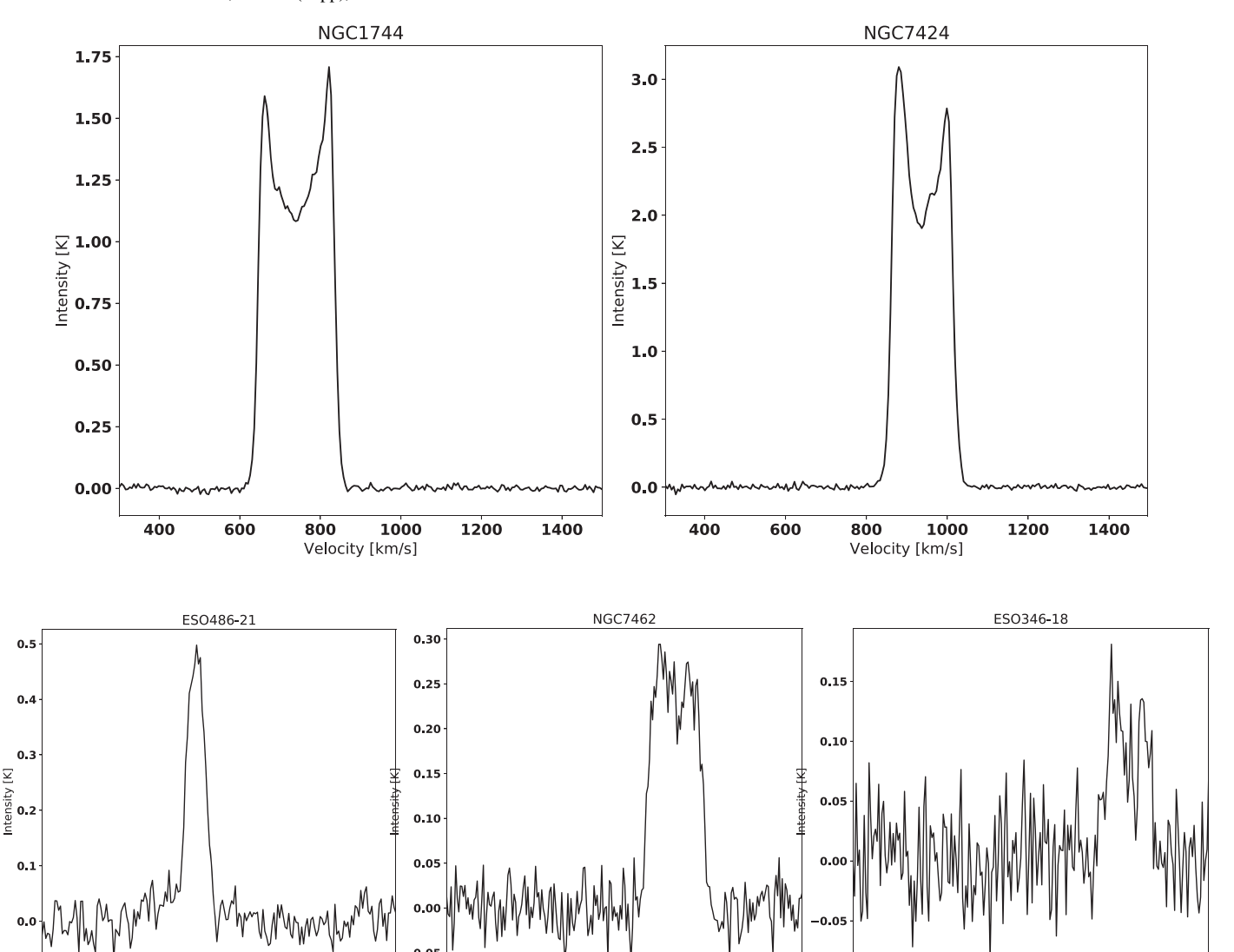


Figure 3. Total integrated H I profiles. Top row: NGC 1744 (left) and NGC 7424 (right). Bottom row: ESO 486-G021 detected in the NGC 1744 cube (left), and detected in the NGC 7424 cube is NGC 7462 (middle) and ESO 346-G018 (right).

created for each galaxy and can be seen in Figure 3. No other significant detections of H I were seen throughout the cube.

1200

1000 [km/s]

800 Velocity

5. Analysis

Each source in this survey was analyzed by extracting information from the data cubes and deriving individual galaxy properties, followed by creating both masked and unmasked total integrated intensity (moment 0) maps and measuring the global properties of the galaxy environments from these images. Moment 0 maps for each source can be found in S19. In doing this, we can identify the statistical properties over a wide population of galaxies.

5.1. Total integrated H I Flux Profiles

We created total integrated H I flux profiles for each galaxy using the MIRIAD task MBSPECT. MBSPECT makes a measurement of the data cube over a wide velocity range, where channels including emission are masked and a first-order

polynomial is fitted to the baseline, removing residual baseline variation. We obtain the 1σ rms noise over emission-free channel ranges, as well as the total integrated flux, and the line widths of each source at 20% (W_{20}) and 50% (W_{50}) of the peak flux value. These measured values are listed in Table 2. Each galaxy's global line profile can be seen in Figures 7–23.

1200

Velocity [km/s]

5.2. Derived Galaxy Properties

For each data cube, we calculate the per-channel 1σ column density sensitivity. We use measurements from MBSPECT to derive physical properties of each galaxy in the sample, such as the total H I masses, total dynamical masses, and neutral gas fractions.

Column densities are calculated with

$$N_{\rm HI} = 1.822 \times 10^{18} \left(\frac{T_{\rm B}}{\rm K}\right) \left(\frac{dv}{\rm km \, s^{-1}}\right) \rm cm^{-2},$$
 (2)

where $T_{\rm B}$ is the brightness temperature in units of K and dv is the resolution of our data in km s⁻¹. When estimating the detectable

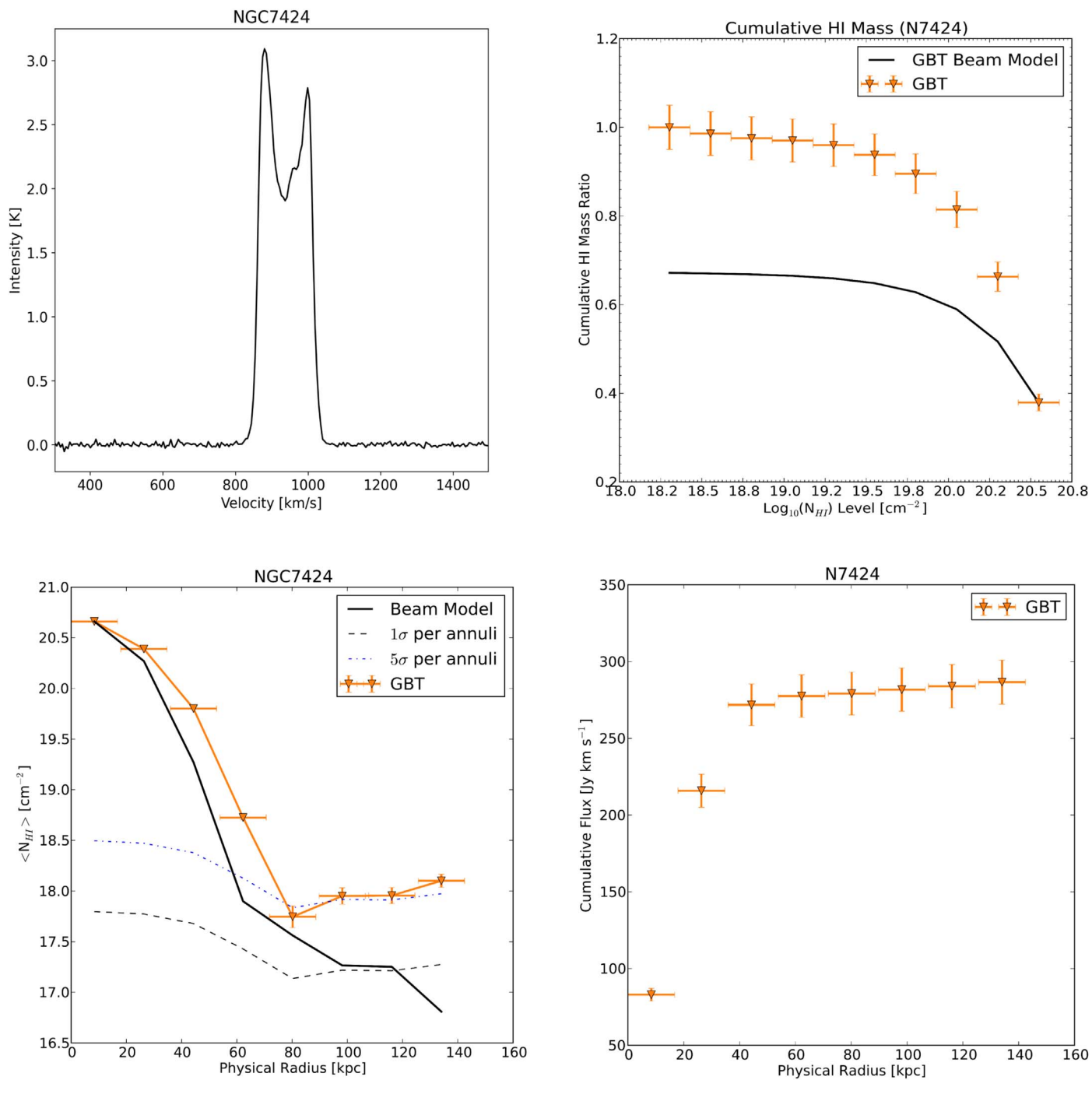


Figure 4. Top left: total integrated H I profile. Top right: cumulative H I mass. The total H I mass in the moment 0 map is plotted by the fraction of gas in column density bins and compared to the GBT beam model, scaled to the peak column density. Bottom left: azimuthally averaged $N_{\rm HI}$. Column density is averaged over annuli extending radially from the center of the galaxy and compared to the GBT beam model. The black dashed line characterizes the 1σ noise in each annulus, and the blue dotted–dashed line represents the 5σ noise in each annulus. Bottom right: cumulative flux. Fluxes in each of those annuli are summed to obtain a measure of the total flux out to the edge of each map.

column density level in the cube, we use a 5σ limit and a minimum line width of a typical H I detection (20 km s⁻¹).

We integrate over the total flux values to estimate the H I mass of each source, assuming that the H I is optically thin, using

$$M_{\rm HI} = 2.36 \times 10^5 \, D^2 \int_{\nu_1}^{\nu_2} S(\nu) d\nu \, M_{\odot}.$$
 (3)

Here the distance, D, is in Mpc, and $\int_{v_1}^{v_2} S(v) dv$ is the total integrated flux over velocities enclosing the H I profile v_1 to v_2

and is in units of Jy km s⁻¹. The brightness temperatures from each cube were divided by the $1.86 \, \mathrm{K} \, \mathrm{Jy^{-1}}$ gain of the GBT to obtain units of Jy. We calculated this gain using an aperture efficiency of ~ 0.65 (Boothroyd et al. 2011) for the GBT at 1420 MHz.

In order to calculate the total dynamical mass of each galaxy, we first calculated the physical H I diameter, $D_{\rm H~I}$, using the Broeils & Rhee (1997) scaling relation (Equation (2.5)), which is dependent on the optical diameter of the galaxy, D_{25} ,

measured at the 25th mag arcsec⁻² isophote in the B band. We used values for D_{25} from the Lyon–Meudon Extragalactic Database (LEDA). We use the dynamical mass equation:

$$M_{\rm dyn} = 2.3 \times 10^5 \left(\frac{v_{\rm rot} / \sin(i)}{\rm km \, s^{-1}} \right)^2 \left(\frac{r}{\rm kpc} \right) M_{\odot}, \tag{4}$$

where $v_{\rm rot}$ is the rotation velocity in km s⁻¹ and i is the inclination, also taken from LEDA. These properties obtained from NED and LEDA can be seen in Table 1. We use our line width at 20% maximum to estimate $v_{\rm rot}$ as $v_{\rm rot} = W_{20}/2$. Dynamical masses are calculated inside the H I radius, r in kpc, calculated as $D_{\rm H\,I}/2$.

The last property we derive using the information at hand is the neutral H I fraction. This is defined as the fraction of H I mass in the galaxy and is calculated with $f_{\rm HI} = M_{\rm HI} / M_{\rm dyn}$. Each of these derived properties is listed in Table 2 for every galaxy in the sample.

5.3. GBT Beam Model

One of the main science goals of this survey is to detect low column density H I around our sample of galaxies. In order to distinguish between low column density H I from an extragalactic source and the low-level radiation entering the sidelobes of the GBT's main beam, we use a beam model that measures these sidelobe levels precisely, modeling the beam response of an unresolved point source. We adopt the beam model used by Pingel et al. (2018). Without this model, emission entering the nearest sidelobes from the main beam could be confused for low column density emission from our sources. For each source in our sample, we used the GBT beam model as a template to regrid each data cube to have $4^{\prime\prime}$ pixels with size 1024×1024 using the MIRIAD tasks IMGEN and REGRID.

5.4. Integrated Intensity Images (Moment 0)

We created integrated intensity images, or moment 0 images, for each source in our sample. An unmasked image was made by integrating pixel values over a channel range in the data cube containing emission from the central source. We also created masked moment 0 images with the intention of separating signal from noise when searching for low column density H I. In order to do this, we set to zero the pixels with values below three times the noise in that cube and again integrate over the same channel range. After integration over the channel range we selected, we expect the $\sigma_{\rm rms}$ noise in each map (masked and unmasked) to increase by a factor of

$$\sigma_N = \sqrt{N} \ \sigma_{\rm rms},$$
 (5)

where N is the number of channels integrated over and $\sigma_{\rm rms}$ is the rms noise per channel in the data cube. We calculated a 1σ noise map for both the masked and unmasked images this way. We then create our maps using a 3σ cutoff in the same way as Pingel et al. (2018) by creating a signal-to-noise ratio (S/N) map for both the masked and unmasked images. The S/N map for the unmasked image is made by dividing the unmasked integrated image by the unmasked 1σ noise map, while the masked S/N map is created by dividing the image where pixels below $3\sigma_{\rm rms}$ were set to zero by the masked 1σ noise image. From each of these S/N maps, we calculated a 3σ threshold by

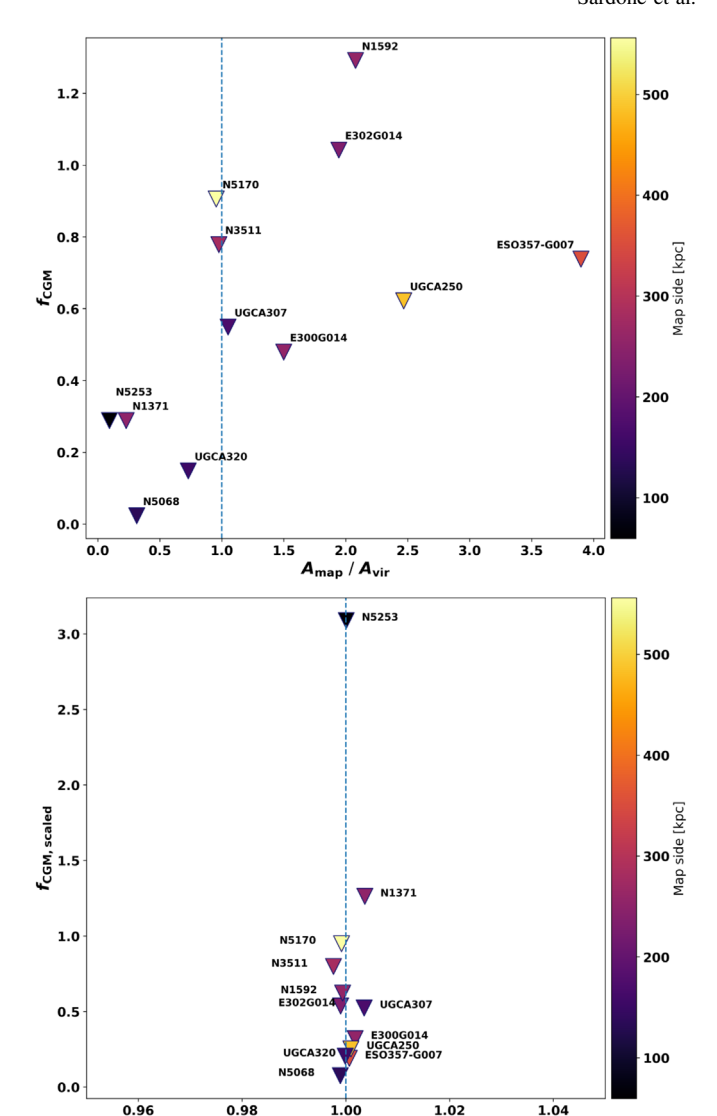


Figure 5. Top: amount of H I detected in the CGM as a fraction of the H I disk mass. These CGM mass measurements were taken throughout the map area and are shown relative to the target galaxy's virial area. The color bar identifies the physical size of the map. The blue dashed line indicates a map area equal to the virial area. Bottom: fraction of mass in the CGM in the top panel, now scaled such that each map area is equal to its virial area. Triangles offset for visual ease.

taking the mean value of the pixels with S/N values falling between 2.75 and 3.25. We then use this new 3σ value to mask, or set to zero, the pixels in our masked integrated image that fall below this value. In doing this, we are confident in our characterization of the noise in our maps.

5.5. Cumulative H I versus N_{HI}

We want to find out how much HI mass is contained at different column density levels in each galaxy. In doing this, we will be able to identify the amount of low column density HI in the galaxy as a percentage of the total HI mass. Accordingly, in the way described in Pingel et al. (2018), we bin the column densities above the 3σ level in our unmasked image and calculate the percentage of HI mass that falls into each $N_{\rm HI}$ bin by converting each pixel in the image to a column density level, and subsequently into an HI mass. We determine

the percentage of H I mass at or above a given column density bin and can therefore quantify the percentage of H I mass below some column density threshold. Each galaxy is normalized to that galaxy's maximum H I mass in the cumulative H I versus $N_{\rm HI}$ plots in Figures 7–23.

In addition to the data from each cube, we use the beam models described above to determine whether each source can be reliably analyzed. Each beam model for each galaxy is scaled to the maximum column density of the associated GBT image from the data, and we analyze it in the same way as the GBT images described in the previous paragraph, calculating the cumulative H I mass in each $N_{\rm HI}$ bin. In doing this, we can determine whether the source is following the response of the GBT beam or deviating from it. If the source follows the beam, we can determine that the source is unresolved and therefore does not satisfactorily fill the beam, causing the HI column density to spread out over the beam area and appearing as if low column density HI was detected. To this end, we would omit these unresolved sources from our statistical analysis of the disk. We distinguish which sources are unresolved by looking at the cumulative HI mass ratio of the data versus the model. If the data follow the beam response of the model, we determine that source to be unresolved. Data points above the model are characterized as resolved, and if the error bars fully clear the beam model, we categorize it as very well resolved.

We can infer additional information about the amount of low column density H I in the galaxy by looking at the shape of the profile in relation to the GBT beam model. If a source contains excess diffuse H I, we will see a positive deviation in the data at low column densities as compared to the beam model. Several of the resolved sources follow the shape of the beam model, and they flatten out at or above the 3σ column density threshold described in Section 5.3, which is indicative of the scarcity of low column density H I in that galaxy. If, instead, we see an increase at low column densities as compared to the beam model, then we know that we are detecting an excess of low column density H I within that halo, which could be diffuse gas or clumpy material spread over the beam. This excess could be the result of a number of scenarios, including detection of a low column density companion, extended or clumpy H I clouds, the presence of a $> 3\sigma$ noise artifact, or the detection of accretion of low column density H I from the CGM. For each image showing a higher fraction of low column density HI, we search for $> 3\sigma$ artifacts in order to rule out that possibility, and we look for higher-S/N regions in both the cubes and the integrated images.

5.6. Radial N_{HI}

We also want to determine how H I column densities ($N_{\rm HI}$) behave as a function of distance from the galaxy. The optimal way of identifying abundances in low column density H I is to take the average of the H I column density levels in annuli around the galaxy. This allows us to characterize the azimuthally averaged $N_{\rm HI}$ at various physical galaxy radii. We define the annuli for each galaxy using the masked rather than unmasked images so as to reduce the effect of quantifying low-level noise as signal. Each image is regridded to have 1024×1024 pixels, corresponding to 4'' pixel $^{-1}$ for the purpose of precision when quantities inside each annulus are calculated. The GBT beam's FWHM of 9!1 sets a lower limit to the radius of the smallest annulus to be 4!5, or \sim 68 pixels. The maximum radius of the largest annulus is calculated as the

Table 3 H I Depletion Timescales

Source	SFR	log M _{disk} ^{HI}	$ au_{ m disk}^{ m gas}$	f_{19}	
	$(M_{\odot} \text{ yr}^{-1})$	(M_{\odot})	(Gyr)		
(1)	(2)	(3)	(4)	(5)	
ESO 300-G014	0.063	9.12	28.41	0.44	
ESO 300-G016		8.0		0.93	
ESO 302-G014	0.038	8.65	15.98	0.64	
ESO 357-G007	0.041	9.05	37.46	0.60	
KK 98-195	•••	7.71		0.72	
KKS 2000-23	•••	8.73		0.72	
NGC 1371	0.427	9.95	28.41	0.17	
NGC 1592	0.079	8.36	3.92	0.83	
NGC 1744	0.195	9.62	29.08	0.09	
NGC 3511	0.447	9.55	10.8	0.21	
NGC 5068	0.288	9.33	10.08	0.07	
NGC 5170	0.589	10.29	45.03	0.14	
NGC 5253	0.525	8.09	0.32	0.30	
NGC 7424	0.372	10.11	47.16	0.05	
UGCA 015	0.001	7.12	24.18	0.83	
UGCA 250	0.603	10.09	27.77	0.22	
UGCA 307	0.031	8.75	24.75	0.43	
UGCA 320	0.021	9.27	121.21	0.18	

Note. SFRs obtained from Leroy et al. (2019). Column (3) lists the H I mass of the disk. Column (4) lists the gas depletion timescales for the disk gas, including a correction for helium mass. Column (5) lists the diffuse neutral fraction of gas below $N_{\rm HI}$ < 10^{19} cm⁻².

largest multiple of the 68-pixel radius that lies within the image size. For most of our sources, we calculate this to be eight annuli, and for images in which we use a smaller region around the galaxy, we end up with five annuli. The $N_{\rm HI}$ within each annulus is then averaged by summing the values greater than 3σ and dividing this by the total number of pixels in the annulus. Dividing by the total, rather than the number of pixels above 3σ , we run the risk of underestimating the average $N_{\rm HI}$ in the annulus, but we are avoiding a bias toward higher $N_{\rm HI}$ values that would result from the average using only values $> 3\sigma$.

Once again, we want to be able to compare the data against the GBT beam model to look for deviation from the response of the beam. Each model is scaled to the maximum $N_{\rm HI}$ value in the image and drops off at larger radii. The galaxies in our sample follow the response of the beam at low radii and begin to flatten out around the 3σ threshold. Some of the galaxies flatten out above this threshold, which could indicate a smooth extent of the galaxy rather than an ionization edge at a particular column density level around that galaxy. The 1σ and 5σ thresholds are indicated for each galaxy as the dashed horizontal lines in Figures 7–23.

We can also infer details about the environments of these galaxies by looking at the shape of the radial $N_{\rm HI}$ profile. If the data follow the noise levels out to large radii, we can then say that there is no low column density H I surrounding that galaxy for levels at or above the rms noise sensitivity reached in that cube. However, several of the galaxies show a positive deviation in the averaged $N_{\rm HI}$ at these large radii. For each galaxy in which this positive deviation is identified, we investigate the cube and integrated maps in order to identify a source for the excess H I. The excess could be due to detection of a companion, an extended H I cloud, a higher σ noise spike, or the accretion of H I onto the galaxy from the CGM.

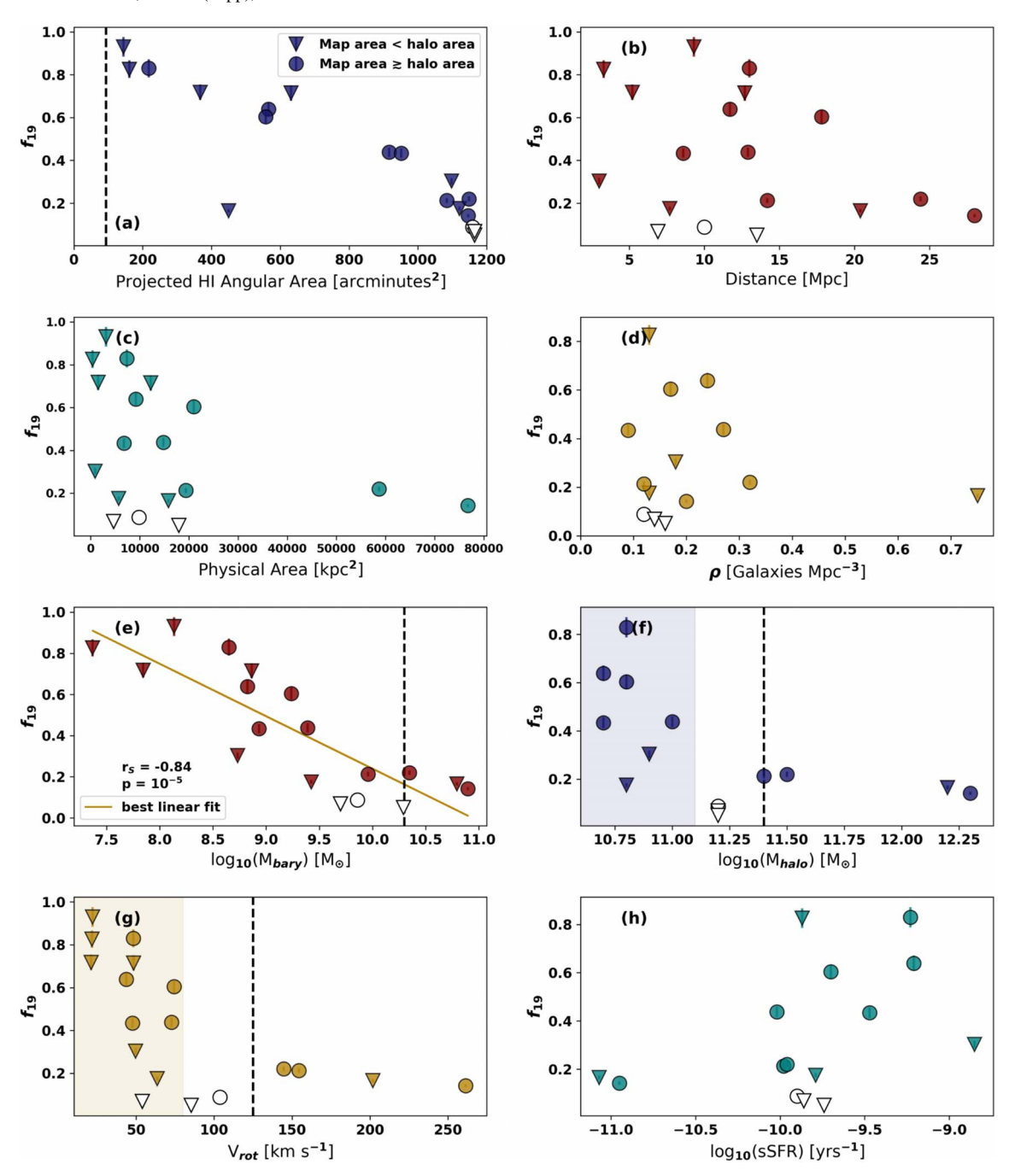


Figure 6. Comparisons of the diffuse neutral fraction for each GBT-MHONGOOSE galaxy. Circles represent measurements over an area larger than or equal to the area of the halo. Triangles represent measurements over a region smaller than the halo and should be interpreted as a lower limit. The two galaxies whose cumulative flux profiles flatten at large radii, indicating that the H I has truncated, are shown as open symbols. (a) Angular areas calculated inside the region where column densities reach $N_{\rm HI} > 1 \times 10^{19}$ cm⁻². The vertical dashed line represents the angular area of the 9.1' FWHM GBT beam. (b) Distance. (c) Physical areas calculated from the $N_{\rm HI} = 1 \times 10^{19}$ cm⁻² angular diameter. (d) Galaxy density. (e) Baryonic mass using $M_{\rm bary} = 1.36 \cdot M_{\rm HI} + M_{\ast}$. The vertical dashed line is at the cold accretion threshold given in Kereš et al. (2005). We show a best-fit line through the data revealing, rather than a firm threshold for cold accretion, a correlation between a galaxy's baryonic mass and its diffuse gas fraction. The strength of this correlation is demonstrated with the Spearman correlation coefficient and the associated p-value. (f) Dark matter halo mass derived from the Moster et al. (2010) relation. The vertical dashed line is at the threshold also given in Kereš et al. (2005). The shaded region marks a lower threshold showing, based on low- $N_{\rm HI}$ measurements from this work, the regime in which cold accretion is more likely. (g) Rotation velocity using $V_{\rm rot} = W_{20}/2$. A vertical dashed line at 125 km s⁻¹ shows the threshold suggested by Kannappan et al. (2013), below which galaxies become dominated by their gas. We mark a shaded region, based on this work, demonstrating a lower threshold for a diffuse-gas-dominated regime below 80 km s⁻¹. (h) The sSFR calculated using the SFR from Leroy et al. (2019).

5.7. Radial Flux

We can trace the flux in each galaxy out to the same physical radii that we explored in the radial $N_{\rm HI}$ analysis using the same method to calculate each annuli. We use the unmasked images for this analysis, as this is the best way to characterize the total

flux of the galaxy at various radii, since our unmasked images contain all the flux detected from the source.

Since we are measuring the cumulative flux at physical radii, we should see the profile continue to increase linearly as the area inside each annulus increases linearly if the average $N_{\rm HI}$

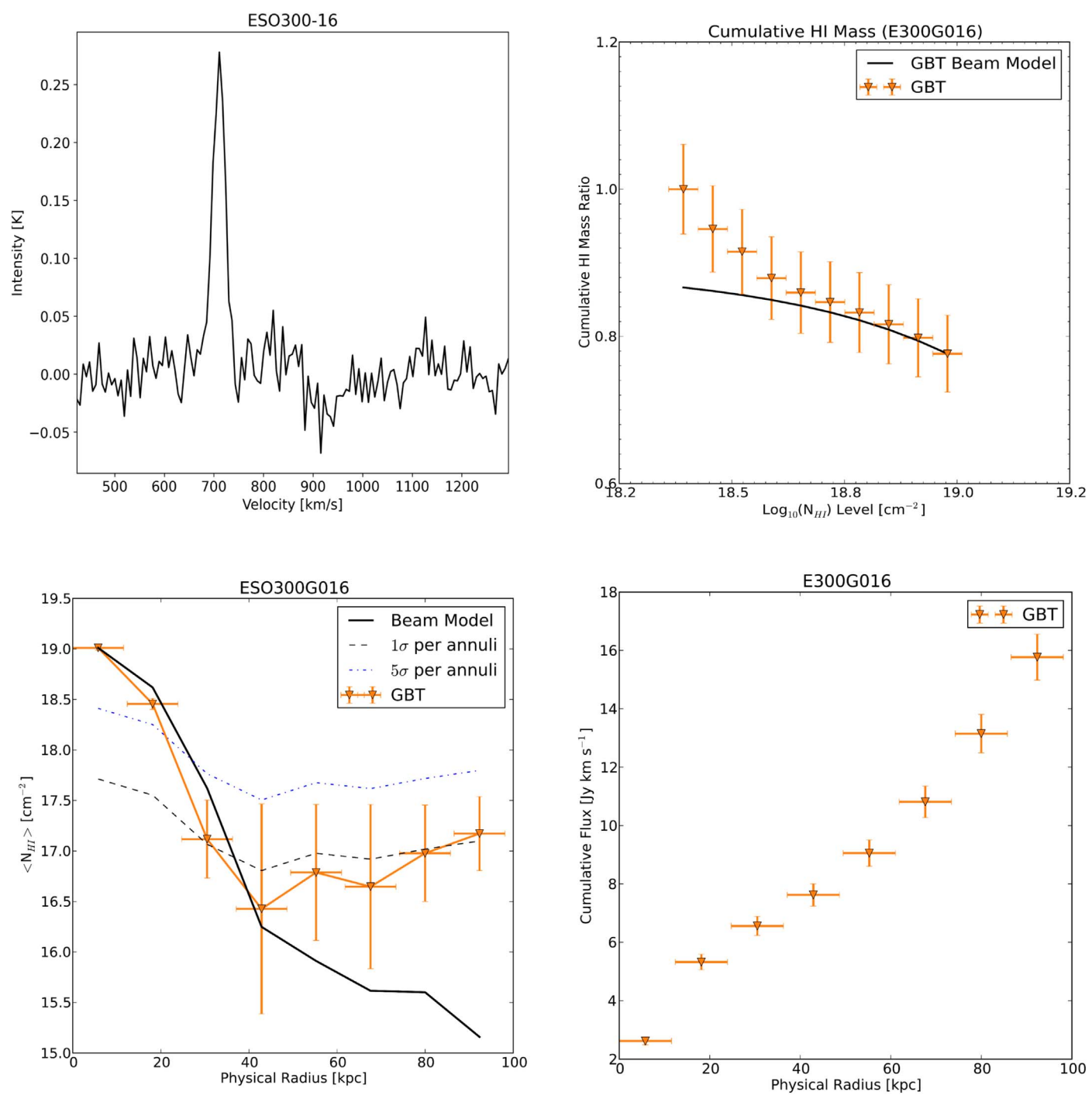


Figure 7. Same as Figure 4, but for ESO 300-G016.

described above is flat. If the radial flux profile deviates from a positive linear trend, we know to look for an increase in low column density gas around that galaxy. A dip in the profile is likely indicative of an unphysical negative feature in the image, causing the cumulative flux to decrease at that radius. If indeed we see rising cumulative flux levels at increasing radii, these would be consistent with the detection of H I at large impact parameters as is seen in Das et al. (2020), where H I is detected at each point along the minor axis out to $\sim 120 \, \mathrm{kpc}$.

6. Results

Most of the galaxies in our sample are moderately to well resolved in the GBT beam and give us reliable statistical properties. As described in Section 5.5, a resolved source is defined by a positive offset of the data from the GBT beam model in the cumulative H I mass versus $N_{\rm HI}$ plots and in the radially averaged $N_{\rm HI}$ versus physical radius plots. The plots in Figures 7–23 show, clockwise from top left, the total integrated H I profile versus velocity, the cumulative H I mass versus $N_{\rm HI}$, the cumulative flux

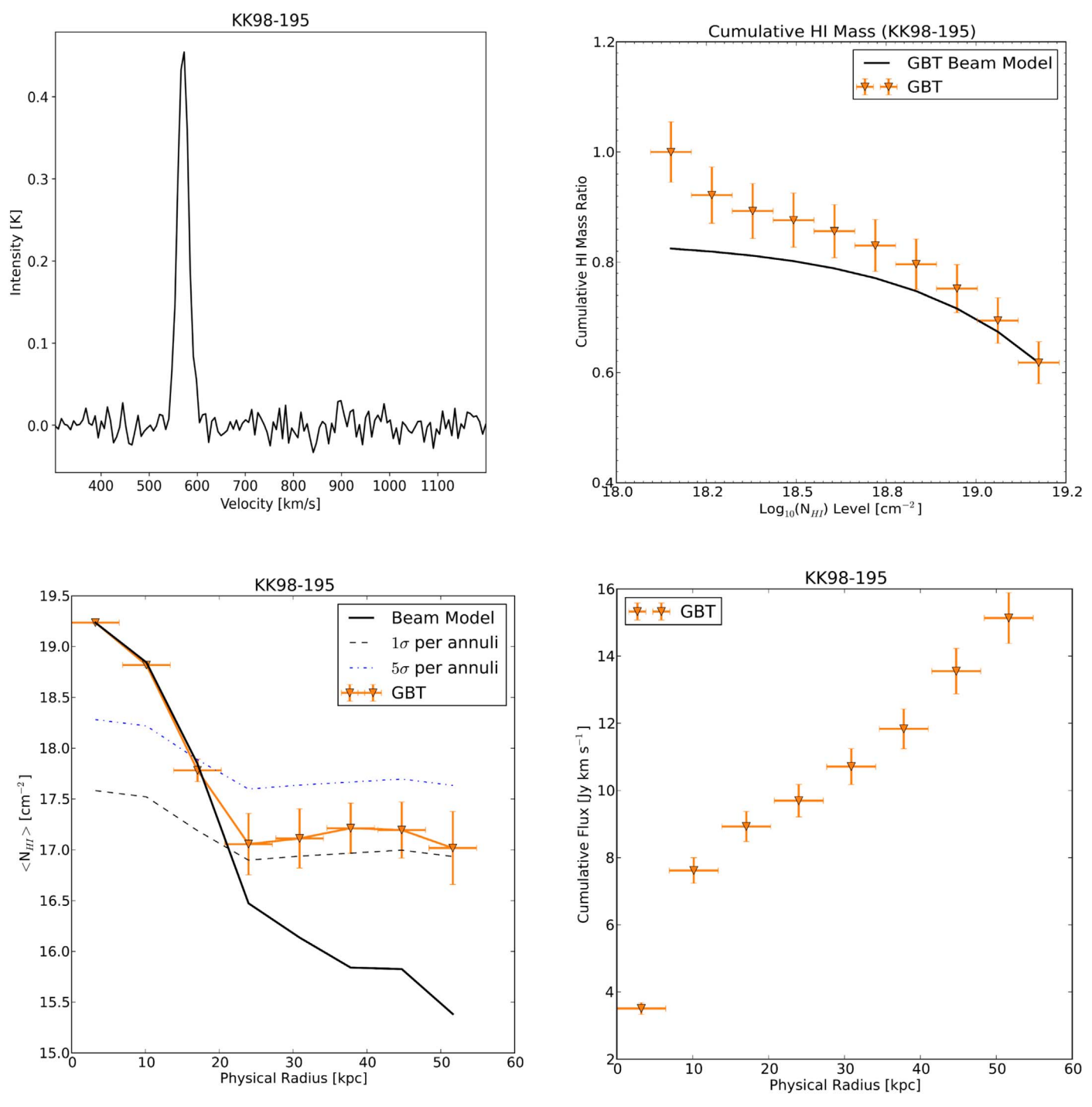


Figure 8. Same as Figure 4, but for KK 98-195.

versus physical radius, and the azimuthally averaged $N_{\rm HI}$ levels versus physical radius. For reference, we have put this analysis for NGC 7424 in Figure 4, while the remainder of the analysis for each galaxy in our sample can be found in the Appendix. The results from analysis of all of our sources will be described below, and they have been grouped by low (bin 1), intermediate (bins 2–5), and high (bin 6) H I mass displayed in Figure 1.

6.1. Low
$$M_{HI}$$
 (6 < $\log_{10}(M_{HI})$ < 8 M_{\odot})

Figure 7 displays a very slight positive offset of ESO 300-G016 from the GBT model in the cumulative H I mass versus

column density, where the lowest column density levels deviate in the positive direction. At the smallest radii seen in the radially averaged $N_{\rm HI}$ plot, we can see that this source is not well resolved until we move beyond the disk, where our underestimated $N_{\rm HI}$ values are consistent with the noise and begin to rise. The cumulative flux continues to rise even at large distances from the disk.

We see that the response of the data in the plots of KK 98-195 (Figure 8) is fairly unremarkable. We see a very slight positive deviation of the cumulative H I mass as compared to the GBT beam model at the lowest $N_{\rm HI}$ level, demonstrating a small fraction (less than 10%) of the H I mass in the galaxy to

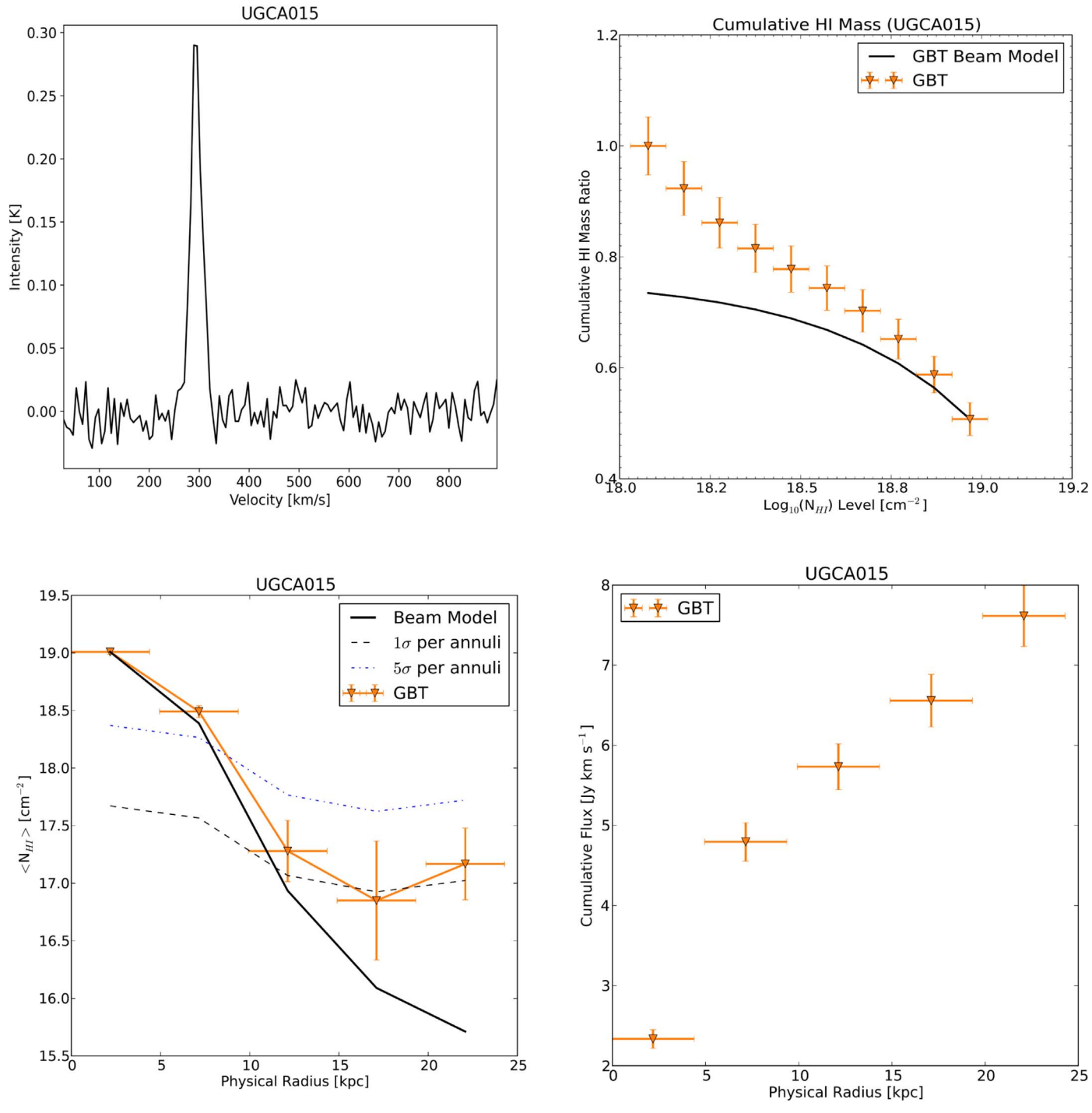


Figure 9. Same as Figure 4, but for UGCA 015.

be at the lowest column densities. The average $N_{\rm HI}$ flattens outside the disk in the radially averaged $N_{\rm HI}$ plot, and the flux increases linearly in the cumulative flux plot.

UGCA 015 (Figure 9) is \sim 40′ in angular distance from the large galaxy, NGC 247, which shows up in our data cube at overlapping velocities. For this reason, we analyzed a smaller region around UGCA 015 in order to exclude possible emission from NGC 247. We see a positive offset in the H I mass at the lower column densities. While we were not able to extend out to farther radii, we note that the cumulative flux again does not begin to flatten beyond the disk.

Peak column densities in each of these low- $M_{\rm HI}$ galaxies sit right around $N_{\rm HI}=10^{19}\,{\rm cm}^{-2}$. None of the three galaxies in this mass range display any positive deviation from the noise level in the azimuthally averaged $N_{\rm HI}$ plots, but each one shows an increase in the fraction of H I mass at the lowest column densities. The largest of these fractions comes from UGCA 015, where the offset from the beam model deviates significantly, making up over 20% of the mass fraction from the lowest column densities. Each of the radially averaged cumulative flux profiles continues to rise as far as our maps reach. This indicates that we have not yet reached the end of the H I emission in our maps of these smallest galaxies.

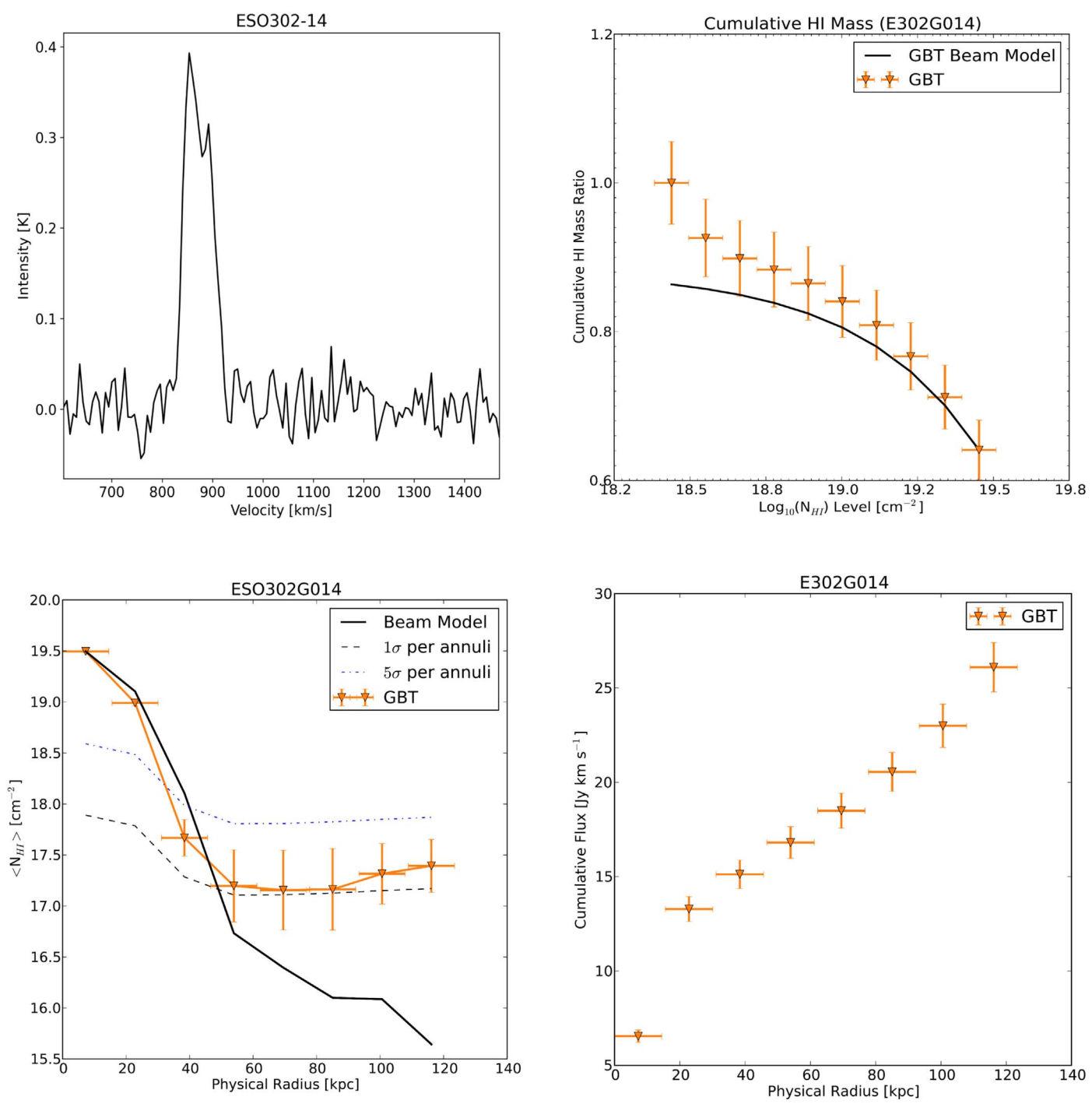


Figure 10. Same as Figure 4, but for ESO 302-G014.

6.2. Intermediate M_{HI} (8 $< log_{10}(M_{HI}) < 10~M_{\odot}$)

Figure 10 displays the properties of ESO 302-G014, where we see an increase at the lowest column densities in the cumulative H I mass plot, flattening outside the disk in the radially averaged $N_{\rm HI}$ plot, and increasing flux levels in the cumulative flux plot. de Blok et al. (2020) detect a filament extending off the disk of ESO 302-G014, as well as an H I cloud with a peak column density of $N_{\rm HI}=4\times10^{19}\,{\rm cm}^{-2}$ about 30 kpc south of the center of the galaxy. These structures are significantly smaller than the FWHM beamwidth of the GBT, and this emission would be spread out over the beam, diluting the signal.

NGC 1592 (Figure 11) has a peak column density level of just over $N_{\rm HI} = 10^{19} \, {\rm cm}^{-2}$. The cumulative flux rises at large radii.

The properties of NGC 5253 are shown in Figure 12. There is an increase in the azimuthally averaged column density levels around 25 kpc, which is associated with one bright region in the integrated intensity (moment 0) image. This bright region has no associated optical counterpart or previously identified H I cloud, nor do the spectra show anything we would consider to be radio frequency interference. Thus, we considered it to be a candidate for accretion of H I onto the galaxy.

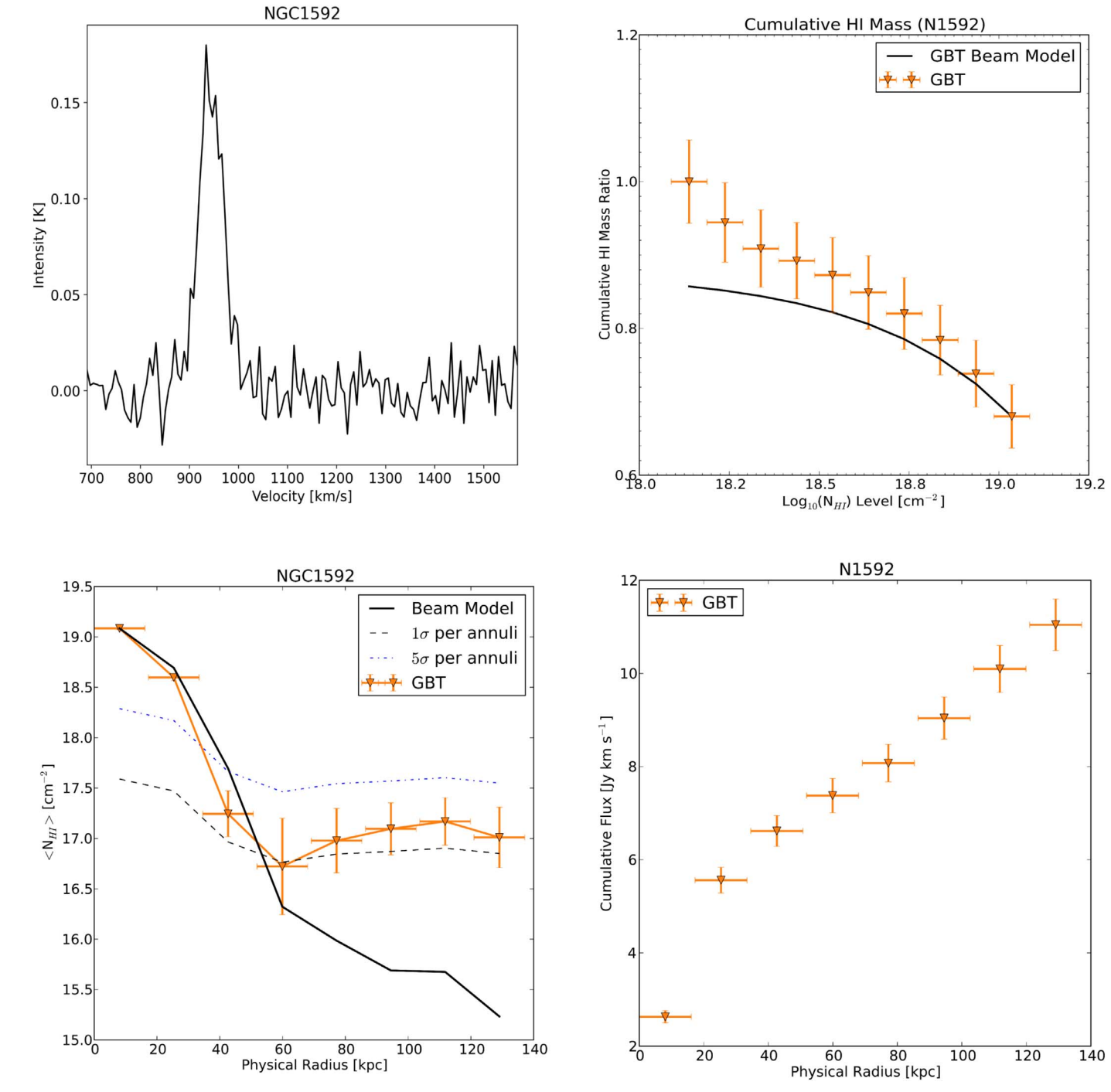


Figure 11. Same as Figure 4, but for NGC 1592.

ESO 357-G007 (Figure 13) contains increasing amounts of diffuse H I beginning around $N_{\rm HI}=10^{18.8}\,{\rm cm}^{-2}$, comprising over 20% of the cumulative H I mass fraction. We can see in the azimuthally averaged $N_{\rm HI}$ plot that the galaxy does not appear to be resolved in the GBT beam at low physical radii of the galaxy and displays an increasing average $N_{\rm HI}$ at the radii beyond the disk. The cumulative flux does show a nonlinear increase at the largest physical radii mapped. In the absence of evidence of a companion galaxy, or any bright artifact in the data cube causing the cumulative flux to increase, we are led to believe that this evidence of excess neutral hydrogen at large radii could be accretion through the CGM onto ESO 357-G007.

Alternatively, this excess of low column density H_I could be indicative of a large reservoir of H_I sitting in the halo of ESO 357-G007.

KKS 2000-23 shows a significant portion of its H I mass to be made up of low column density gas, as can be seen in the cumulative H I mass plot in Figure 14. However, inspection of the data cube and the moment map reveals a higher level of noise in the image, making it difficult to determine whether the low column density gas comes from real emission or is some artifact from the observation. This particular issue could be alleviated with additional observations to verify the presence or absence of low- $N_{\rm HI}$ gas.

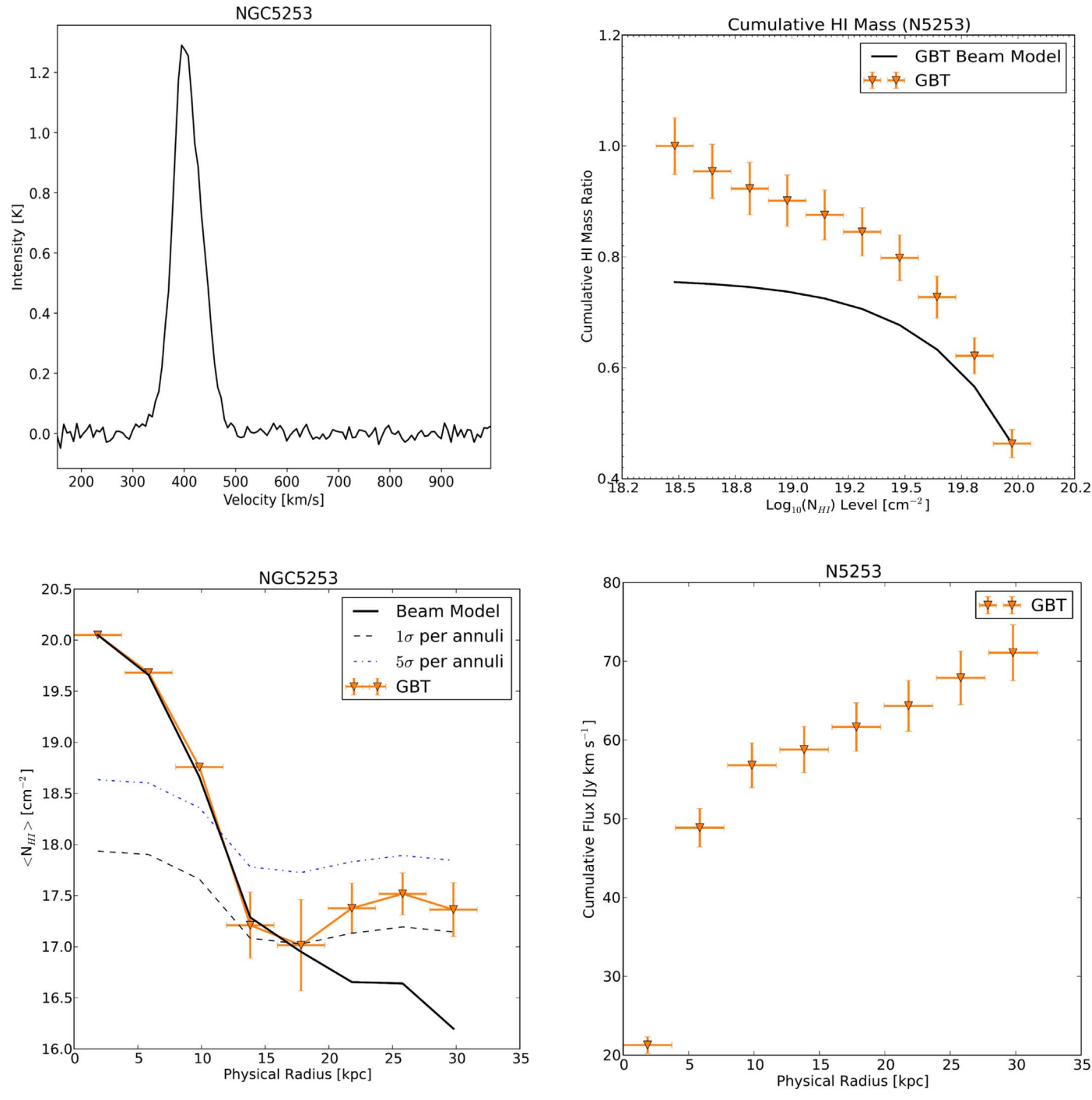


Figure 12. Same as Figure 4, but for NGC 5253.

UGCA 307 also shows an increase in low column density gas in Figure 15. However, the azimuthally averaged $N_{\rm HI}$ versus physical radius displays a steep increase between 55 and 65 kpc. We inspected the data cube and discovered a small galaxy, which we believe is LCRS B125208.8—112329, residing 72 kpc away in projected distance. This can also be seen in the cumulative flux versus physical radius plot, where the flux increases around the same physical distance. This would be the first velocity information available for this galaxy, with a central velocity of 863 km s⁻¹.

The spiral galaxy ESO 300-G014 can be seen in Figure 16. The total integrated flux of ESO 300-G014 displays the

expected double-horn feature for an inclined, rotating galaxy. It is resolved in the GBT beam, where the cumulative flux follows the shape of the GBT beam model, and is positively offset in relation to that model. The azimuthally averaged column densities versus physical radius show a rising $N_{\rm HI}$ level outside the disk, and the cumulative flux at increasing physical radii increases linearly.

Similarly, the face-on galaxy NGC 5068 exhibits similar behavior when comparing these same properties. The cumulative H I mass plot in Figure 17 shows that \sim 99% of the mass in the galaxy is seen in column densities above $N_{\rm HI}=10^{19}\,{\rm cm}^{-2}$. This is substantiated in both the average $N_{\rm HI}$ and

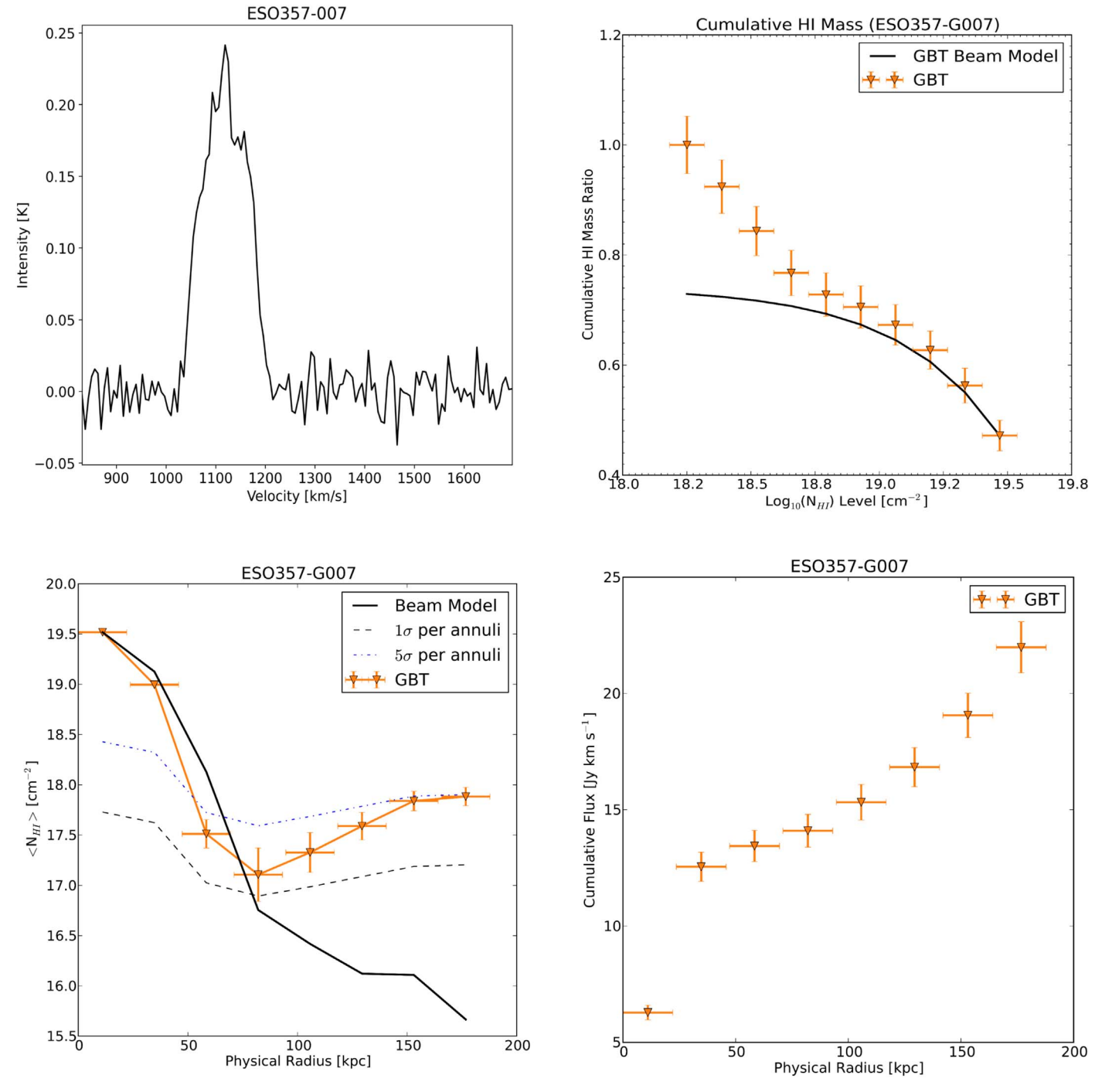


Figure 13. Same as Figure 4, but for ESO 357-G007.

cumulative flux versus physical radii plots, where there is no evidence of an increase in H I gas at large radii.

We detected two additional sources in the region close to UGCA 320: UGCA 319 at \sim 41 kpc, and a second detection around \sim 61 kpc projected distances. The closer companion, UGCA 319, can be seen as a slight bump in the averaged $N_{\rm HI}$ around \sim 45 kpc in Figure 18. The second H I detection lacks a known counterpart in H I but may be associated with the small galaxy LEDA 886203, the only optical galaxy near this position. These two companions are likely what is causing the gradual increase in cumulative H I flux at radii larger than

 $40\,kpc.$ This would also be the first redshift information available on LEDA 886203 with a central velocity of $727\,km\;s^{-1}.$

NGC 1371 is well resolved in the GBT beam, as seen in the cumulative H I mass plot in Figure 19. In most of these plots, NGC 1371 behaves as expected, with the exception of an artifact at \sim 150 kpc as seen in the radially averaged $N_{\rm HI}$ plot.

One of our more massive galaxies, NGC 1744, shows no signs of excess amounts of low column density gas as seen in the cumulative H I mass plot in Figure 20. We can see in the radially averaged $N_{\rm HI}$ plot that this source is well resolved and

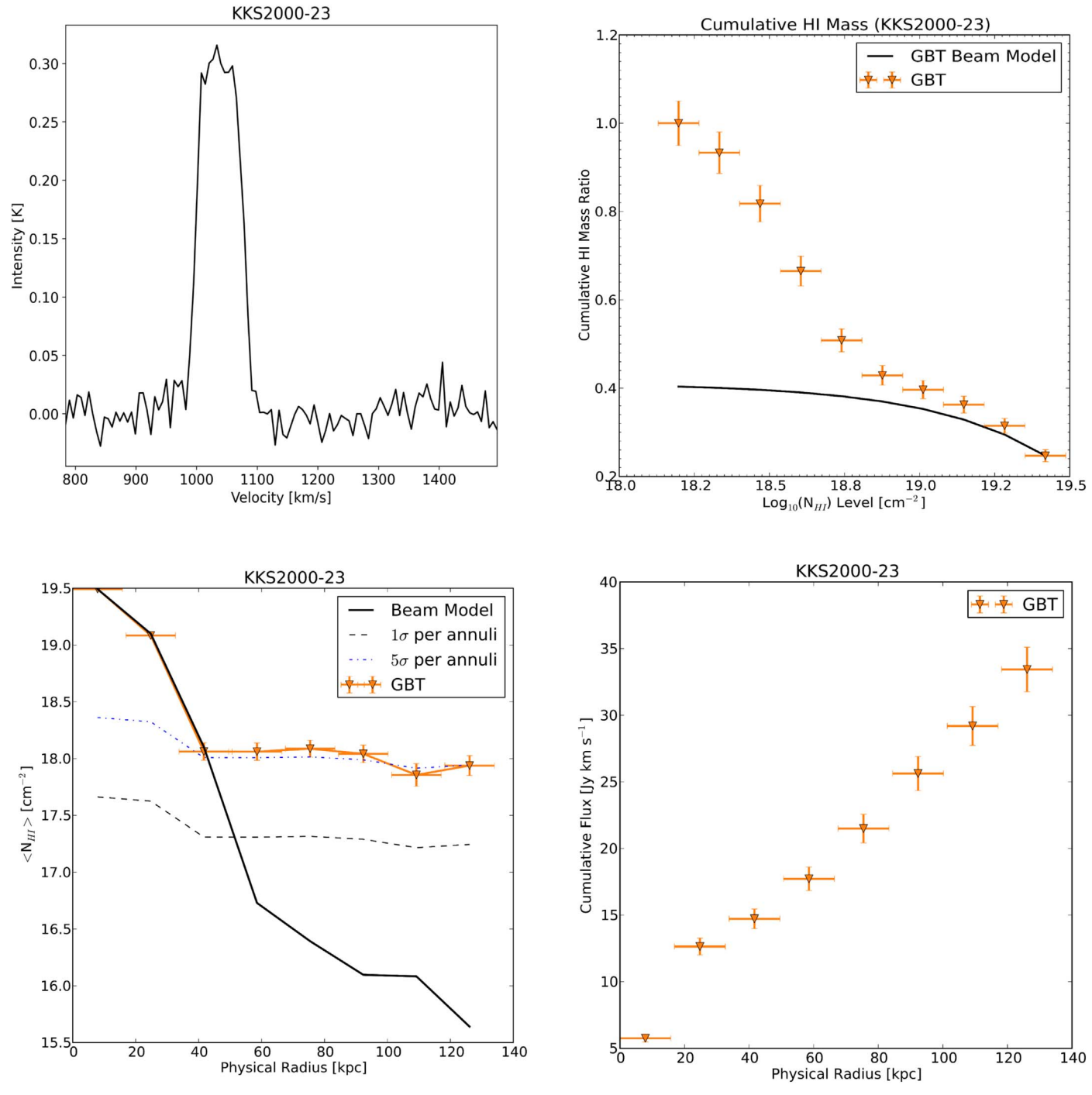


Figure 14. Same as Figure 4, but for KKS 2000-23.

shows an unusually high average $N_{\rm HI}$ at radii beyond the disk. This could be indicative of smooth accretion of H I, a reservoir of H I halo gas, or a higher noise floor than we had estimated.

NGC 3511 (Figure 21) shows large deviation at low column density levels, where the cumulative amount of H I increases almost linearly through $N_{\rm HI} = 10^{18.6} \, {\rm cm}^{-2}$. It is resolved in the GBT beam as seen in both the cumulative mass plot and the averaged $N_{\rm HI}$ plot. Similar to NGC 1744, this source displays higher $N_{\rm HI}$ values out into the halo.

NGC 5170, in contrast with NGC 1744, which resides in the same mass bin, does show an increase toward lower column density H I mass. Figure 22 reveals a sharp change in the slope of

the cumulative H I mass at column densities lower than $\sim 10^{19.4}\,\mathrm{cm}^{-2}$. The azimuthally averaged N_{HI} plot does show an increase in average N_{HI} around 175 kpc. Inspection of the moment 0 image reveals some bright, filamentary structure at the same physical distance, which could be accreting H I gas. Without any indication of a nearby optical counterpart associated with those bright regions that appear to lack optical counterparts, we consider this a candidate for accretion from the CGM.

6.3. High
$$M_{HI}$$
 (10 < $\log_{10}(M_{HI})$ < 11 M_{\odot})

We can see NGC 7424, one of the most H I massive galaxies in our sample, in Figure 4. The data in the averaged $N_{\rm HI}$ versus

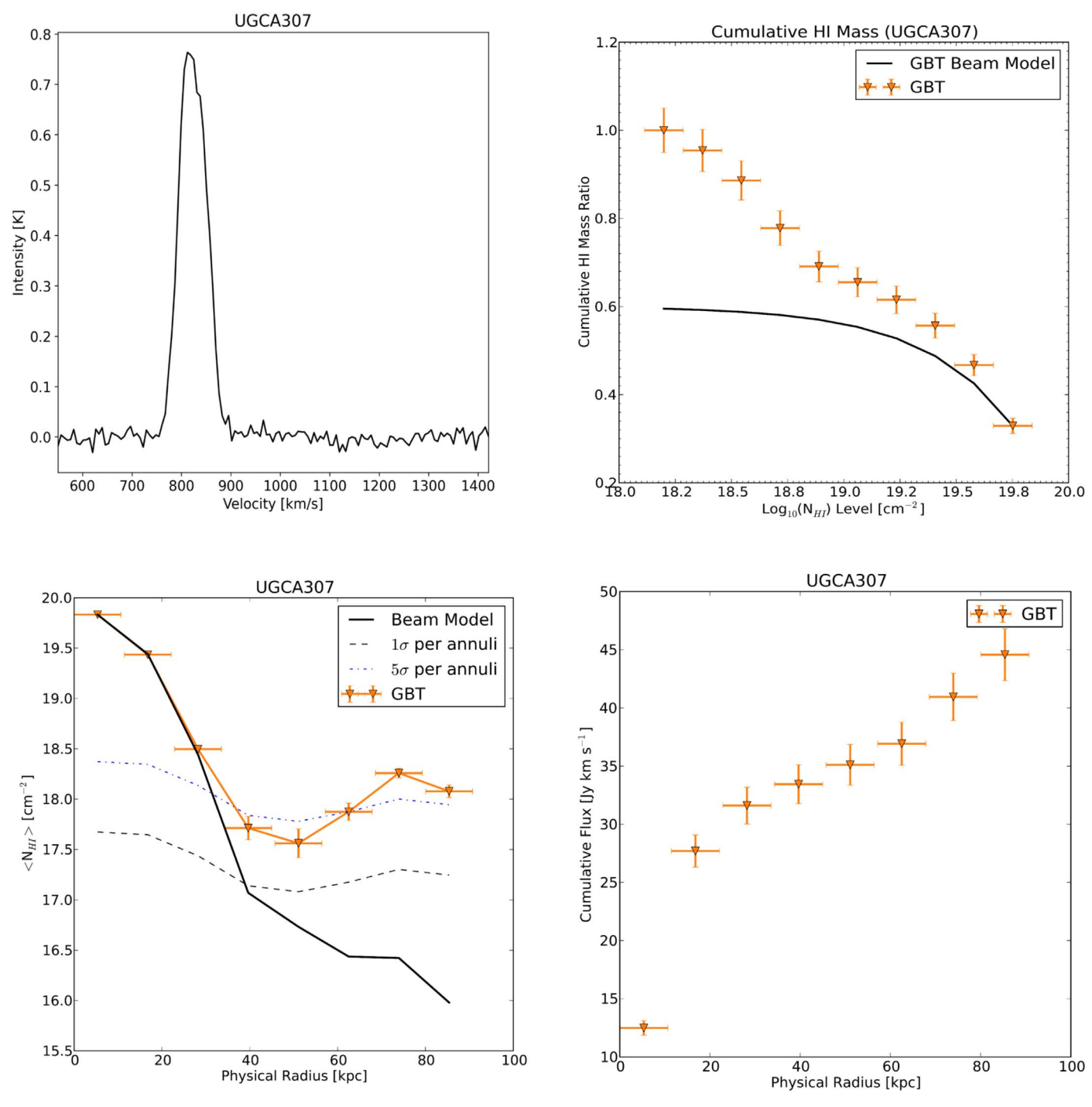


Figure 15. Same as Figure 4, but for UGCA 307.

physical radius plot shows slightly higher and gradually increasing values of $N_{\rm HI}$ at radii outside the disk. Visual inspection of the image did not reveal any regions of particular interest.

One of our largest sources, UGCA 250 (Figure 23), occupies our highest mass bin: $10 < \log_{10}(M_{\rm HI}) < 11~M_{\odot}$. The cumulative H I mass increases at low column densities, and the cumulative flux continues to grow linearly as the radius increases. Inspection of the data cube revealed a bright, positive stripe across the top of UGCA 250, at the same decl. as another bright source on the edge of our cube, UGCA 247. Within that stripe is a possible new H I detection that is coincident with the

only cataloged galaxy within the size of the GBT beam at this position, FLASH J115508.00–282045.1 at a radius of $\sim\!\!185\,kpc.$

7. Discussion

7.1. H I in the CGM

Our analysis of the cumulative HI mass allowed us to quantify the total HI mass in the moment maps. Our maps were made at a constant angular size of $2^{\circ} \times 2^{\circ}$, so we do not have a consistent physical region around each mapped source where initial map sizes range from 105 to 977 kpc on one side. The

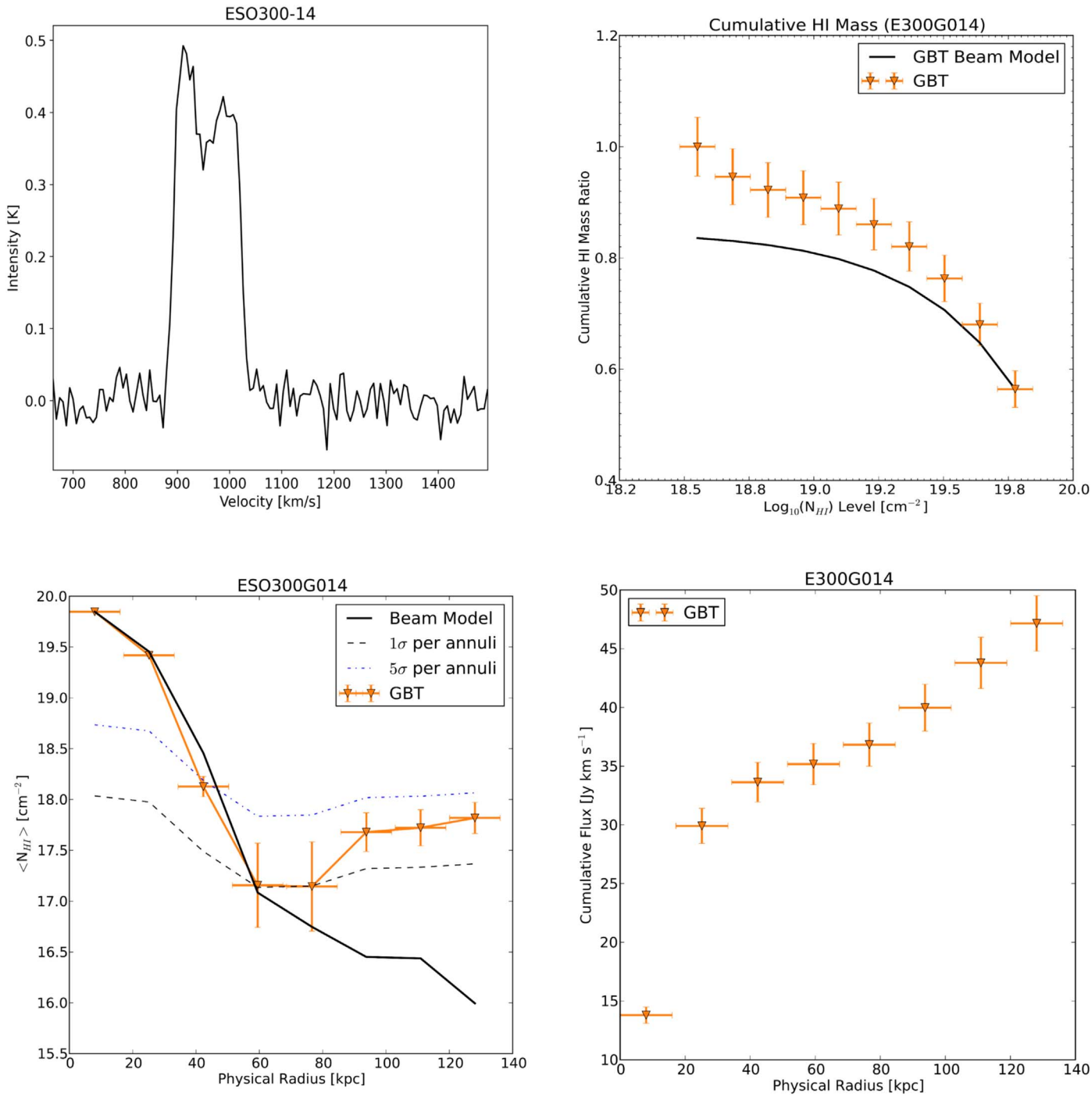


Figure 16. Same as Figure 4, but for ESO 300-G014.

measurement of the H I mass is made in the moment map, where we can subtract off the H I mass of the disk, which is derived from the integrated spectra of each galaxy. The total H I mass in the moment map minus the integrated H I disk mass from the spectra gives us some value for the amount of mass outside the disk. We refer to this amount as $f_{\rm CGM}$. This fraction represents the total amount of H I mass in the CGM in relation to the H I disk mass: $f_{\rm CGM} = M_{\rm CGM}/M_{\rm disk}$. Out of our 18 galaxies, 16 contained an excess amount of gas outside their disk by 0.02-3 times the amount of H I in the disk. The only two galaxies for which we did not detect H I in their CGM were NGC 1744 and NGC 7424. We can see this in both the

cumulative H I mass plots and the cumulative flux plots for both of these galaxies. In both of these galaxies, the cumulative H I mass stays mostly flat at column densities below its turnover ($N_{\rm HI} \lesssim 10^{19.5} \, {\rm cm}^{-2}$), and the cumulative flux does not rise at large distances from the galaxy. This same flattening also occurs with NGC 5068, which contains only 2% more H I outside its disk. This tells us that there is very little, if any, low column density gas outside the disks of these three galaxies. We generally find that maps covering a smaller physical area contain a smaller total amount of $M_{\rm HI}$ outside of the disk, and larger physical maps contain a larger total amount of $M_{\rm HI}$ outside of the disk. This may seem like an intuitive

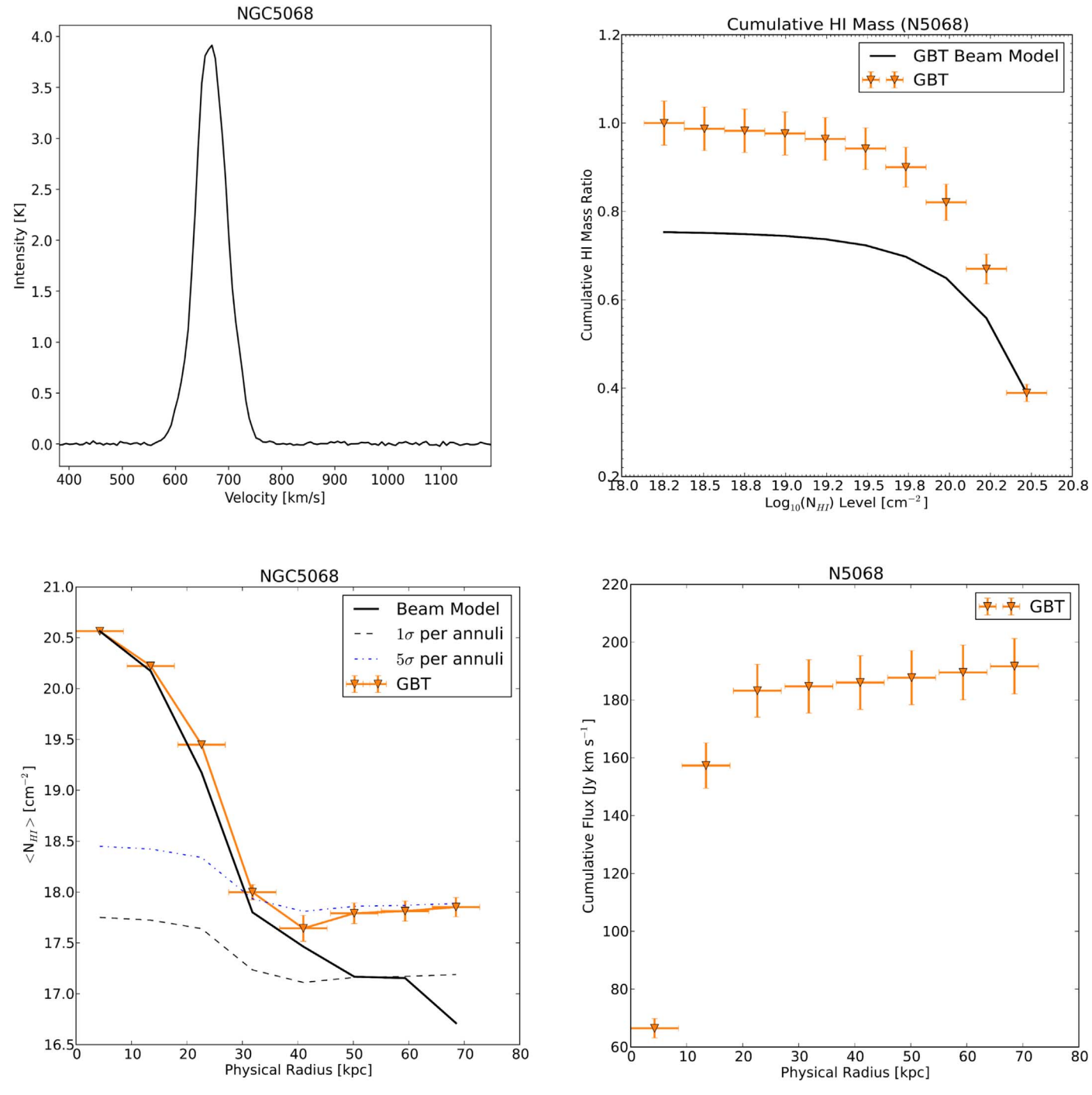


Figure 17. Same as Figure 4, but for NGC 5068.

result if H I permeates the CGM of most galaxies, and yet it has evaded most observational studies of H I emission in the CGM of galaxies. This result is consistent with Das et al. (2020), where H I emission was detected in each measurement at increasing distances along the minor axis of the two galaxies, NGC 891 and NGC 4565. These detections could be the outcome of ubiquitous CGM H I, which, in mapping observations such as this current work, would result in a larger amount of H I detected over larger physical areas. A study of this type could be improved on with a consistent physical parameter guiding the size of the area observed, such as the virial radius of a galaxy. Mapping the full extent of the halo, as the

upcoming Parkes-IMAGINE survey (Sardone et al., in preparation) will do, would give insight into the amount of H I permeating the entire CGM of a galaxy.

As our physical map sizes are not uniform, we would like to know how the fraction of H I mass in the CGM would change, assuming smooth coverage of the gas, if each galaxy were mapped precisely to its virial radius, calculated from the virial mass found using the Moster et al. (2010) stellar-to-halo-mass relation. We show this change in Figure 5, where our empirical measurements are shown in the top panel and a scaled version is shown in the bottom panel. We find that as an increasing fraction of the halo is probed, and in several cases multiple

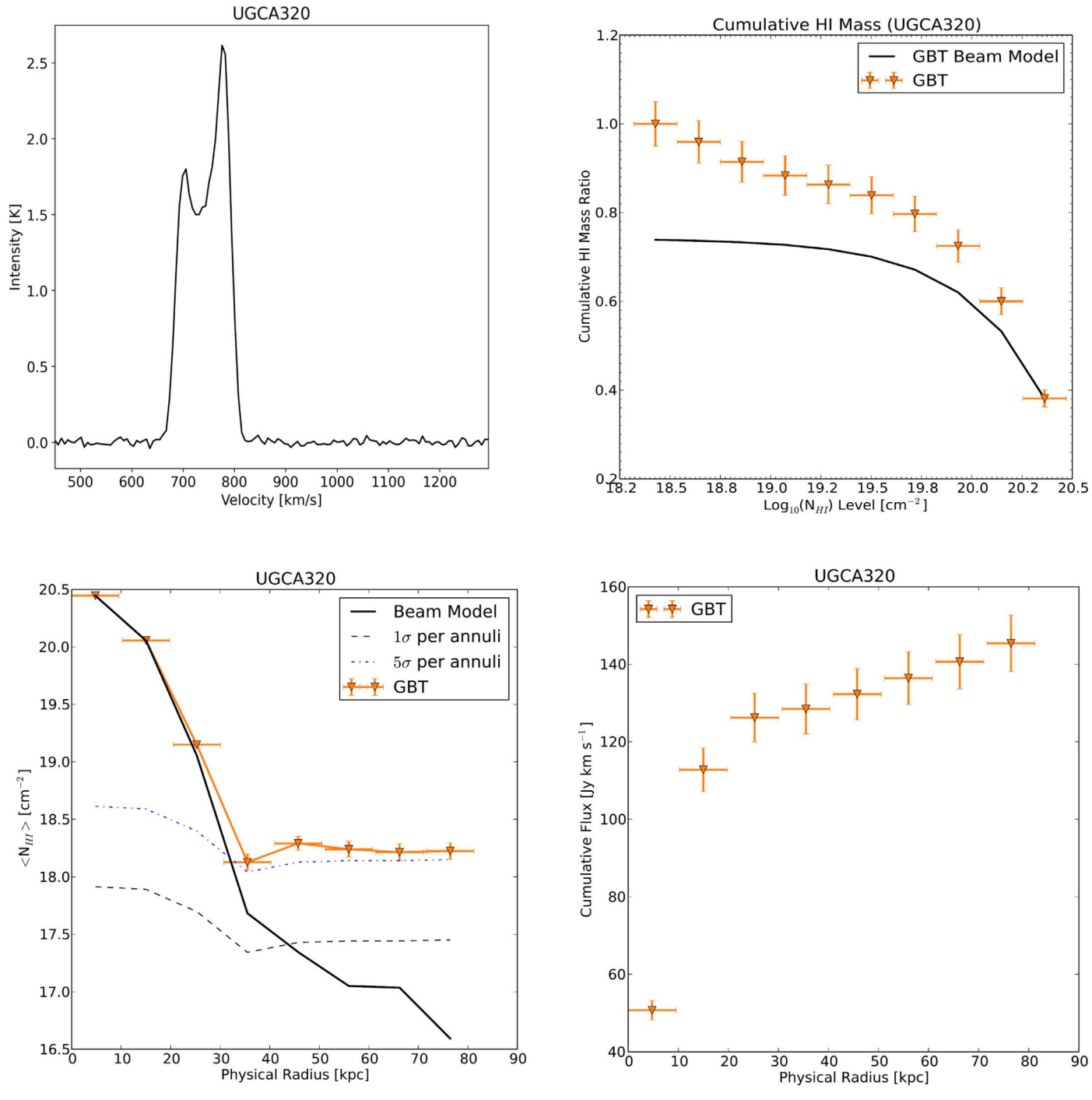


Figure 18. Same as Figure 4, but UGCA 320.

times the halo, the fraction of HIgas in the CGM also increases. The largest value of $f_{\rm CGM}$ comes from the map of NGC 1592. We made measurements over an area twice the size of its halo and found 1.3 times the amount of HI disk mass in the surrounding area. However, when scaling the map to cover precisely one halo area, $A_{\rm map}/A_{\rm vir}=1$, this fraction reduces to 0.62 times the HI disk mass. We note that the scaled fractions, $f_{\rm CGM,scaled}$, reveal an outlier containing three times the amount of HI mass in its CGM, NGC 5253, which we earlier identified as a candidate for accretion. We discuss this further in the following sections.

7.2. Fraction of Low N_{HI}

We define a characteristic column density as low $N_{\rm HI}$ if it is below a level of $10^{19}\,{\rm cm}^{-2}$. This value is taken from the prediction that below $\sim 10^{19}\,{\rm cm}^{-2}$ the amount of hydrogen in the neutral phase is truncated, and the gas transitions from mostly neutral to mostly ionized, making detections much below this level difficult, although not impossible. This sharp drop is largely due to photoionization of the neutral hydrogen by the extragalactic radiation field and represents one way of defining the edge of an H I disk. This was first explained by Bochkarev & Siuniaev (1977) and later by Maloney (1993),

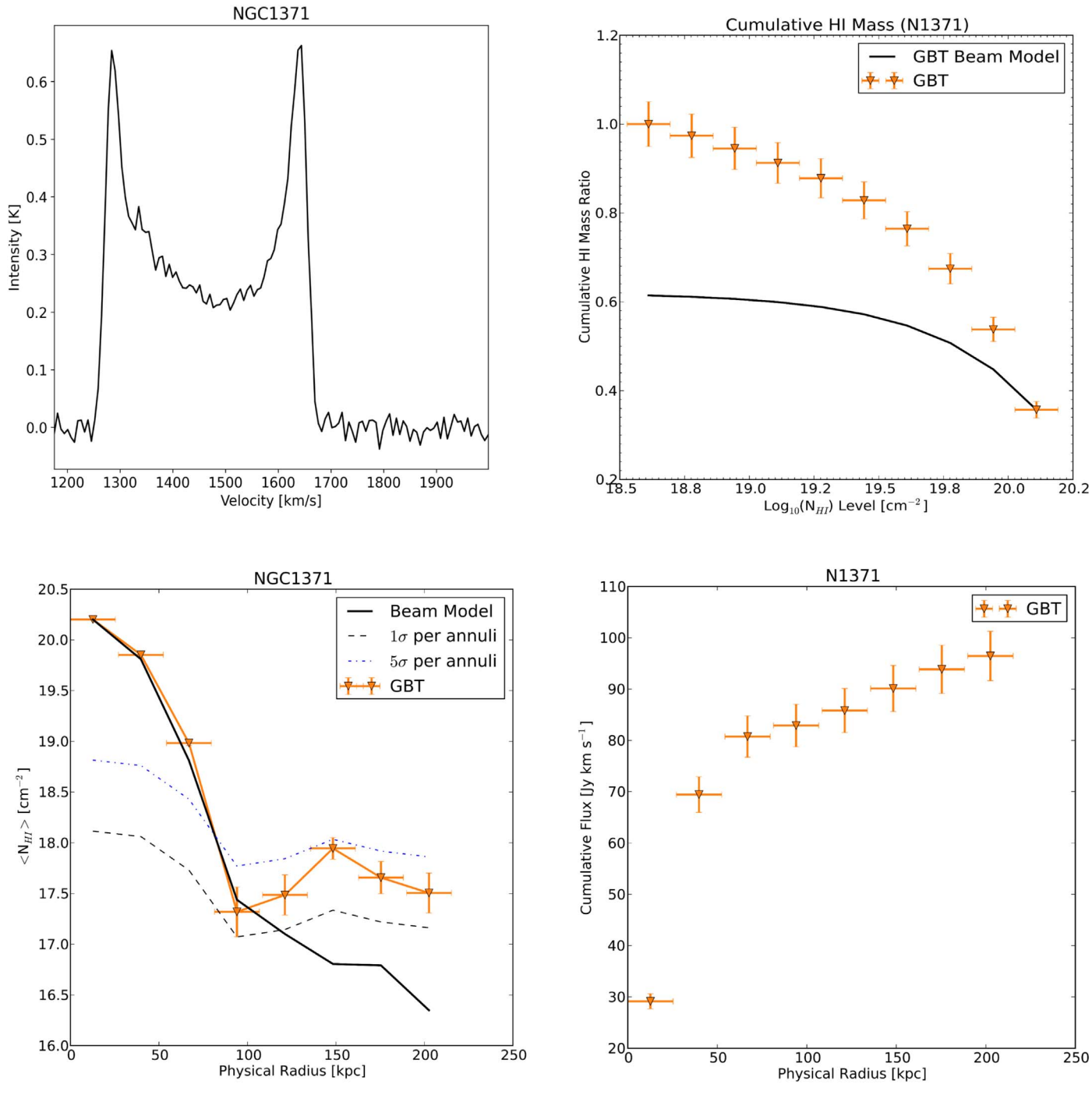


Figure 19. Same as Figure 4, but for NGC 1371.

who suggested that the ionization fraction sharply increases at a critical column density of a few times 10^{19} cm⁻², irrespective of galaxy mass or halo parameters. An example of this sharp drop-off in H I is the KAT-7 observations of M83, which revealed a steep decrease in $N_{\rm HI}$ at the edge of the galaxy disk (Heald et al. 2016). Recently, Bland-Hawthorn et al. (2017) demonstrated that it may be possible to detect low column density H I at significantly larger radii than the predicted truncation radius from Maloney (1993). Specifically, they showed that the radius at which 50% of the total amount of hydrogen is ionized is significantly larger. These results seem to be congruent with those of Ianjamasimanana et al. (2018),

who investigated radially averaged column density profiles of 17 galaxies in search of a break at the $\sim 10^{19}\,\mathrm{cm}^{-2}$ level and found no evidence for a sharp change anywhere above their detection limits.

We determined the diffuse neutral fraction for each galaxy using (Pingel et al. 2018)

$$f_{19} = 1 - \frac{M_{19}}{M_{\rm HI}}. (6)$$

In this equation, the diffuse neutral fraction, f_{19} , is defined by the fraction of H I below column densities of 10^{19} cm⁻², where M_{19} is the H I mass at column density levels $N_{\rm HI} \geqslant 10^{19}$ cm⁻²

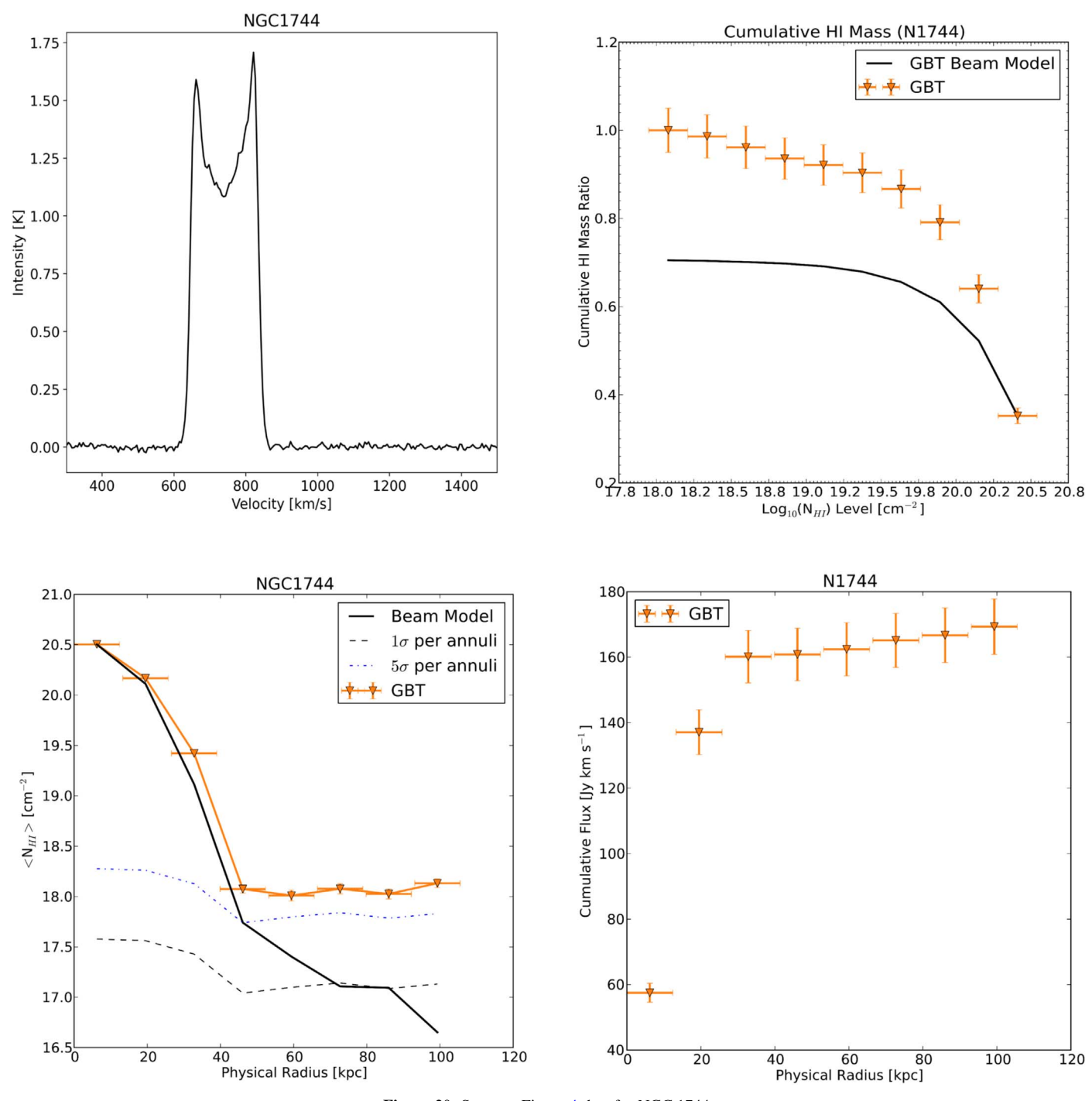


Figure 20. Same as Figure 4, but for NGC 1744.

and $M_{\rm H\,I}$ is the total H I mass as determined in Section 5.5. Values of f_{19} are listed in Table 3.

With our f_{19} values in hand, we would like to compare the diffuse neutral fraction as a function of galaxy parameter, such as galaxy density, baryonic mass, and rotation velocity, and others plotted in Figure 6. We chose these properties in order to make a comparison with theoretical predictions on the relationships between diffuse gas and cold-mode accretion from the IGM.

Our diffuse fractions range from 0.05 to 0.93 of the total H I mass measured in each galaxy. However, as the cumulative flux profile in nearly all of our galaxies continued to rise even

at larger radii, these fractions represent a lower limit. The three galaxies, NGC 1744, NGC 7424, and NGC 5068, in which the H I truncates at some radius have a very low diffuse fraction and are unlikely to change. Eleven of our galaxies are made up of less than 50% diffuse gas. These galaxies are generally our highest H I mass galaxies, demonstrating a perhaps intuitive correlation between mass and diffuse fraction: higher H I mass corresponds to a lower fraction of diffuse H I. This correlation can be seen when we combine the stellar mass and H I mass, or the baryonic mass, in panel (e) of Figure 6.

In panel (a) of Figure 6, we demonstrate the size of the galaxies in relation to the GBT 9.1' FWHM beam area, which

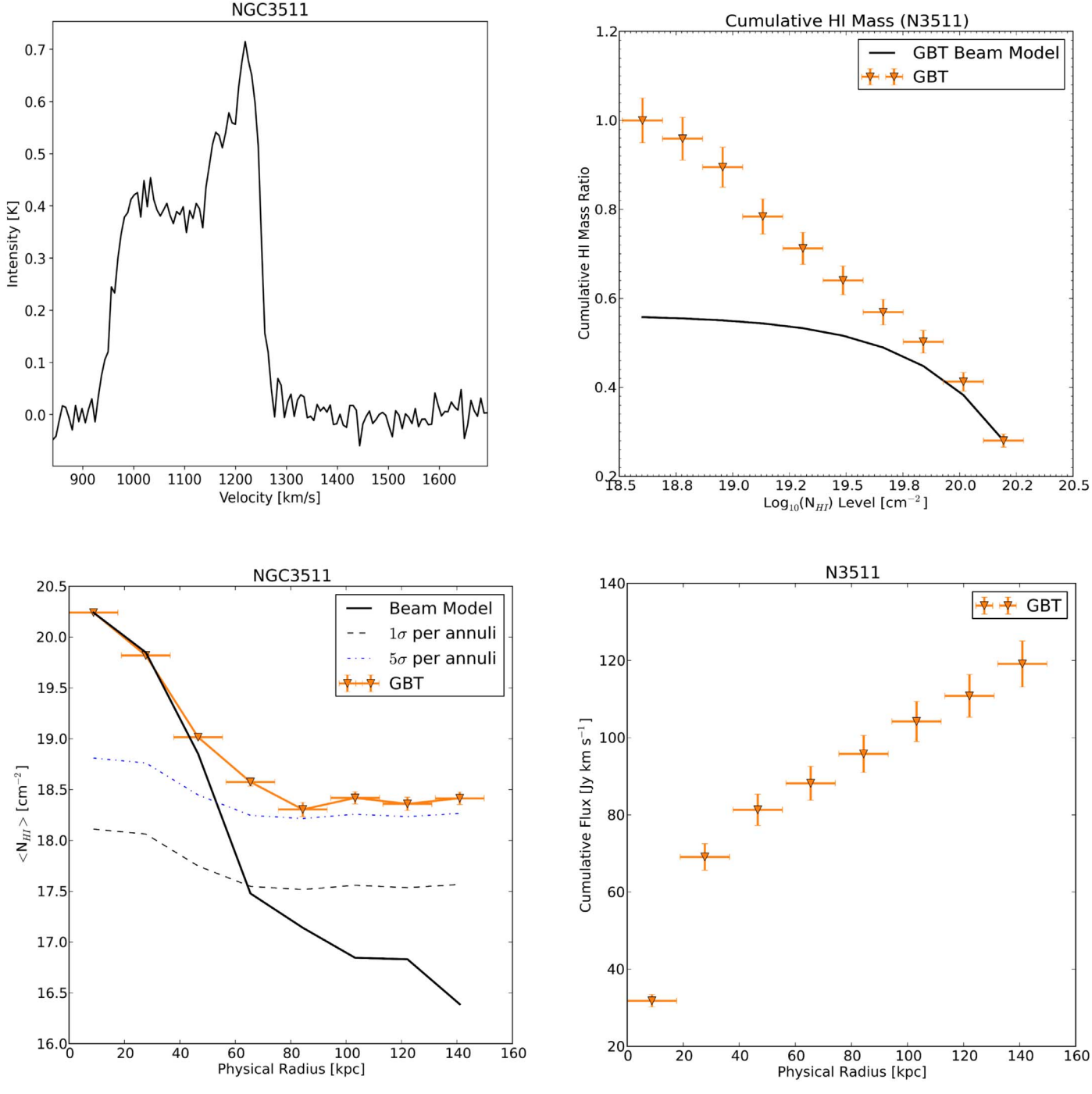


Figure 21. Same as Figure 4, but for NGC 3511.

is illustrated by the dashed vertical line. This helps us determine whether a galaxy is large enough to be considered resolved in the GBT beam, which tells us whether the $N_{\rm HI}$ detected within the beam is representative of the real $N_{\rm HI}$ or is spread out over the beam, diluting the physical $N_{\rm HI}$ values of the galaxy. Each galaxy's area was determined by the number of pixels within the galaxy where column density values were greater than 1×10^{19} cm⁻². We note that the highest f_{19} value, from ESO 300-G016, corresponds to the map with the smallest angular area.

At the largest distances, the GBT's beam covers the largest physical area and could potentially be affected by beam dilution producing unphysically high values of f_{19} . It is clear in

panel (b) that we do not see evidence of high f_{19} values at large distances, or correspondingly large physical map areas. At an intermediate distance of 9.3 Mpc, beam dilution in the map of ESO 300-G016 is not a concern.

Another way to look for this bias toward unphysical low column densities is to plot f_{19} against physical area, which we do in panel (c). Bias in this plot would present as large physical areas with high f_{19} values, due to beam dilution. As we see nothing to indicate any such trend, we are confident that our spatial resolution is suitable for this kind of analysis. We draw attention to the two outlier galaxies in panel (c): NGC 5170 and UGCA 250. These galaxies make up the largest distances in our sample, are the largest and third-largest H I disk masses in our

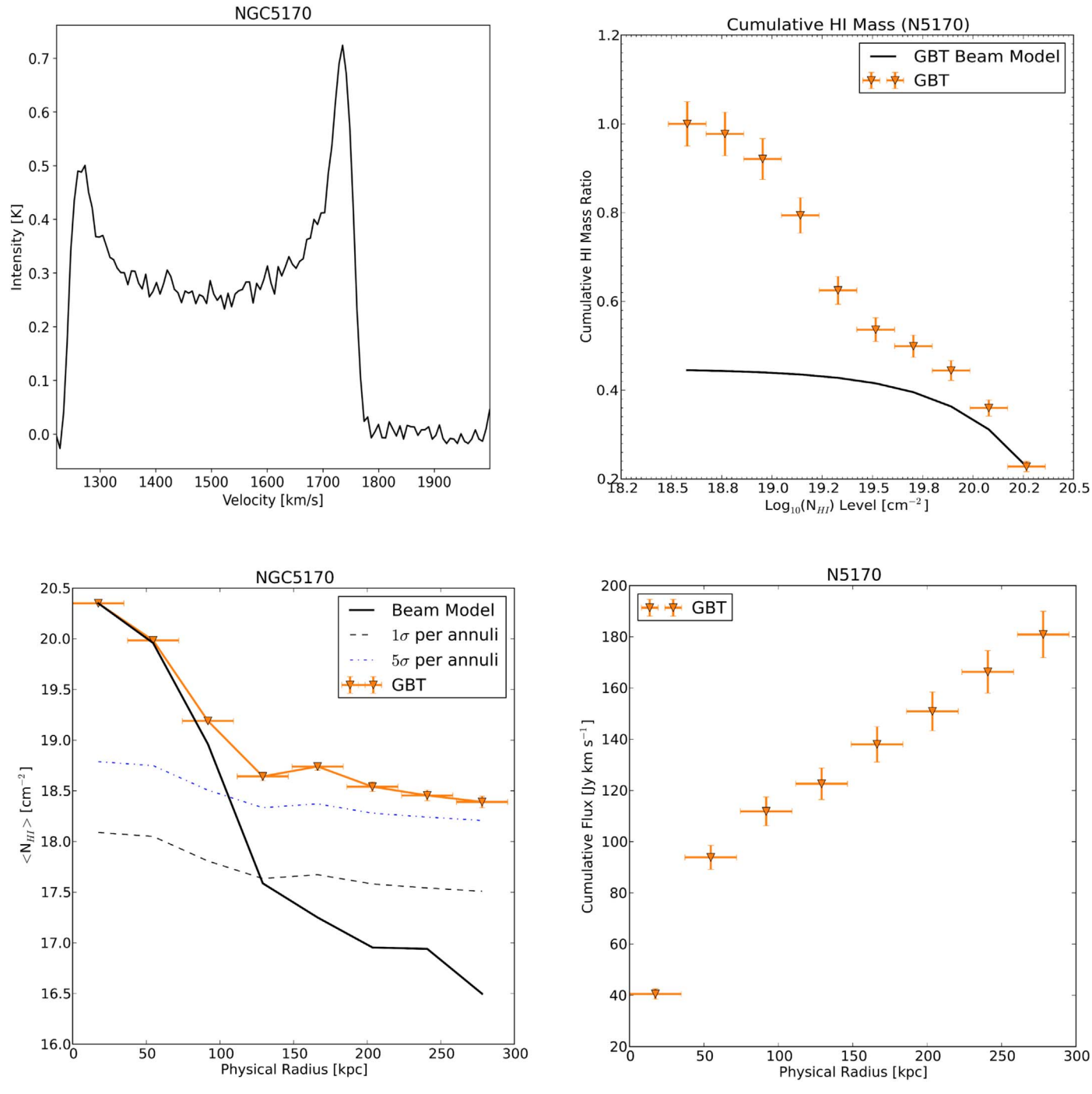


Figure 22. Same as Figure 4, but for NGC 5170.

sample, and contain less than 25% diffuse H I. This is consistent with the general idea that galaxies with larger potential wells are more efficient at bringing halo gas to the disk, leaving less diffuse gas in the CGM. It could also be the result of a hot halo, which is more common around massive galaxies (Kereš et al. 2009), and most of the gas has been ionized, resulting in a smaller neutral fraction.

In panel (d) we look at the environments in which these galaxies live using galaxy number densities from the Nearby Galaxy Catalog (Tully 1988). This catalog identifies the density of galaxies brighter than -16 mag measured in the *B* band within a Mpc³ region of the target source using a 3D grid at 0.5 Mpc spacing. We were unable to obtain galaxy number

densities for four of our galaxies (ESO 300-G016, KK 98-195, KKS 2000-23, and NGC 1592), reducing the size of our sample for this analysis. Regardless, the data we show in panel (d) do not indicate any relation between a galaxy's diffuse H I fraction and its density environment.

In panel (e) we plot f_{19} with baryonic mass for all but three of our galaxies. Kereš et al. (2005) show that cold-mode accretion dominates at baryonic masses ($M_{\rm bary}=1.36\cdot M_{\rm HI}+M_*$) less than $M_{\rm bary}=10^{10.3}~M_{\odot}$. We calculated the baryonic masses using our derived $M_{\rm HI}$ disk value, which was corrected by a factor of 1.36 to account for helium mass, and stellar masses given in Leroy et al. (2019), which provided stellar masses for all but three of our sources. Within our sample of galaxies, we

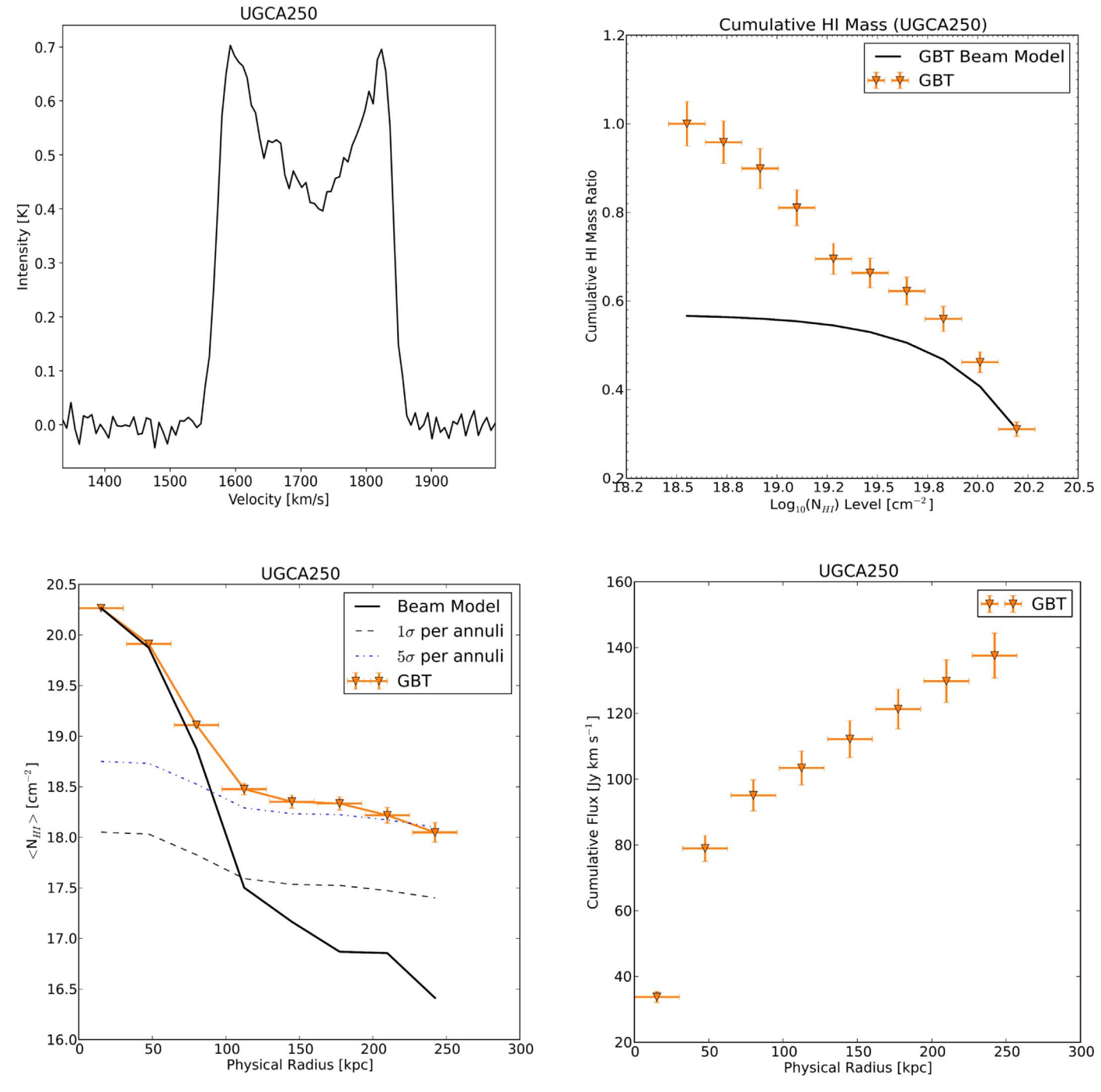


Figure 23. Same as Figure 4, but for UGCA 250.

do find that galaxies with higher fractions of diffuse HIIie entirely below this threshold, complementing the picture of diffuse gas from the IGM flowing directly into galaxies below this mass threshold. However, rather than one mass threshold below which diffuse gas may flow from the IGM, we see a relation between this galaxy mass and the diffuse HI fraction. The trend we see in the comparison of f_{19} with baryonic mass is quantified by performing tests using both the Spearman correlation coefficient and the Pearson correlation coefficient, resulting in nearly identical values of $r_S \simeq r \simeq -0.84$ and a p-value, showing the probability of this correlation occurring by chance, of $p \simeq 10^{-5}$. These tests demonstrate a strong relation between the amount of diffuse HI in a galaxy and that galaxy's

baryonic mass. This observational trend complements the simulations from Kereš et al. (2009), which reveal a smooth trend of increasing cold gas fraction as galaxy mass decreases.

We show dark matter halo masses in panel (f), derived from the Moster et al. (2010) stellar-to-halo-mass relation. In this panel we see that all galaxies with halo masses below $\sim 10^{11.1}~M_{\odot}$ have a spread in diffuse H I fractions, while above this threshold the diffuse fraction remains $\lesssim 0.2$. These data indicate that there may be a dark matter halo mass threshold around $10^{11.1}~M_{\odot}$, above which a galaxy contains less than 25% diffuse H I. We have overlaid a vertical dashed line at the predicted threshold where cold accretion should dominate below $M_{\rm halo} = 10^{11.4}~M_{\odot}$ given in Kereš et al. (2005). Below this halo mass threshold,

we should find larger diffuse fractions associated with those galaxies. The shaded region in panel (f) pushes back this threshold to below $\sim \! 10^{11.1} \, M_{\odot}$.

Rotation velocities are plotted against f_{19} in panel (g), with a distinction being made at the $125\,\mathrm{km\,s^{-1}}$ mark. Kannappan et al. (2013) suggest that this is the threshold below which galaxies are gas dominated. In this regime, galaxies are refueled and have larger gas fractions than those above this threshold. We plot our alternative measurement using f_{19} , which would estimate a "diffuse" gas richness. Once again, while we have a spread of diffuse fraction values below this threshold, supporting the picture of diffuse gas fueling galaxies. We further demonstrate that the data suggest an even lower threshold where galaxies potentially become dominated by their diffuse gas. This is marked in panel (g) by the shaded region below a rotation velocity of $80\,\mathrm{km\,s^{-1}}$.

Panel (h) in Figure 6 is of specific SFR (sSFR) versus f_{19} . We derive sSFR, the SFR per unit stellar mass, using the same stellar masses mentioned above with SFRs derived from UV +IR provided by Leroy et al. (2019). As star formation and galaxy mass are directly related to cold-mode accretion, we want to look for trends in sSFR, as it relates to both. We note in this panel that the highest diffuse fractions tend to fall at the higher end of our sSFR range, which could be contributed to by either inflows into or outflows from the galaxy (e.g., Rubin et al. 2010; Martin et al. 2012; Krumholz & Dekel 2012).

7.3. Depletion Timescales

One method of determining whether nearby galaxies contain enough gas to continue to fuel star formation is to calculate the depletion timescale of the galaxy, given the gas mass and the SFR. This timescale determines how long it will take the galaxy to use up all of its gas if all of this gas is converted into stars. Our depletion timescales are calculated with

$$\tau_{\rm disk}^{\rm gas} = \frac{M_{\rm disk}^{\rm gas}}{\rm SFR},\tag{7}$$

where $au_{
m disk}^{
m gas}$ is the depletion timescale given the gas mass from the disk and $M_{\rm disk}^{\rm gas}$ is the H I mass from the disk, measured from the total integrated HI profiles, corrected for helium with a factor of 1.36. These timescales, listed in Table 3, have a large range of values that fall between 0.32 and 121 Gyr, with a median depletion time of 27.8 Gyr. The depletion timescales we find are consistent with the HI depletion timescales found by both Bigiel et al. (2010) and Roychowdhury et al. (2014). These results tell us that these galaxies currently have enough gas available to them to sustain star formation for well over a Hubble time, with the exception of NGC 1592, NGC 3511, NGC 5068, and NGC 5253, whose values are less than 13 Gyr. In Section 6.2 we noted NGC 5253 as a potential source for accretion. NGC 5253 has been shown to have extremely efficient star formation and streams of metal-enriched dense gas flowing into the starbursting dwarf galaxy (Turner et al. 2015). If NGC 5253 is undergoing ongoing accretion, this, along with its star formation efficiency, could explain the lack of an established reservoir of diffuse HI, as well as its shorter depletion timescale.

8. Summary

We analyzed 21 cm data from GBT observations of 18 MHONGOOSE galaxies to search for diffuse, low column density H I in the CGM of these galaxies. We reached a mean 1σ column density sensitivity of $N_{\rm HI} = 1.3 \times 10^{17} \, {\rm cm}^{-2}$ per channel and a 3σ column density of $N_{\rm HI} = 1.3 \times 10^{18} \, {\rm cm}^{-2}$ over a line width of 20 km s⁻¹.

- 1. By comparing the total HI mass in our maps to the HI measured in just the disk of each galaxy, we determined that 16 out of 18 galaxies contained additional HI mass outside of their disks by an amount of 0.02–3 times as much. This extraplanar or CGM HI was not found in NGC 1744 or NGC 7424.
- 2. We measured the amount of diffuse H I within each map, defined as H I gas with column densities below $N_{\rm HI} = 10^{19} \, {\rm cm}^{-2}$. We compared the amount of diffuse H I with the total H I mass in the map. We found that the galaxies in our sample were made up of between 5% and 93% diffuse H I. If we bin our diffuse fraction values, f_{19} , by quartiles, we find that more galaxies fall into the lowest quartile than any other bin.
- 3. We took measurements of azimuthally averaged H I column densities around each galaxy extending out to the edges of the uniform noise regions in our maps. In 11 of our galaxies, these averaged N_{HI} values remained nearly constant outside the disk region, showing no excess of H I in the averaged annuli throughout the CGM. However, we identified seven galaxies where this column density profile showed some >5σ increase in averaged N_{HI} outside of the galaxy disk. These galaxies are KKS 2000-23, NGC 1744, NGC 3511, NGC 5170, NGC 7424, UGCA 250, and UGCA 320. There are a number of reasons to find a high averaged N_{HI} value outside of the disk, which include detection of a companion (e.g., UGCA 320), or filamentary structure possibly associated with accretion (e.g., NGC 5170).
- 4. We see a rising cumulative flux level at increasing distances in the maps of 15 of our 18 galaxies. This is consistent with our measurement of the H I mass outside the disk, where we find that the same three galaxies (NGC 1744, NGC 7424, and NGC 5068) do not contain any detectable amount of H I mass beyond their disks. This excess mass is seen in the cumulative flux plots where the flux does not flatten at large distances from the galaxy as might be expected if the H I emission drops to zero.
- 5. We compared the fraction of diffuse H I in each map with various environmental properties of our galaxies in Figure 6. We look at particular properties such as baryonic mass, dark matter halo mass, and rotation velocities that have been associated, either empirically or theoretically, with accretion of gas onto galaxies. Most notably, we find a strong correlation between the fraction of diffuse gas and the galaxy's baryonic mass. Using both the Spearman and the Pearson correlation coefficients, we find that these two properties are strongly correlated and have a probability of a chance correlation of nearly zero.
- 6. Simulations such as seen in Kereš et al. (2005) determine a dark matter halo mass threshold below which coldmode accretion is the dominate form of accretion of gas from the IGM onto galaxies. Our results indicate a lower

threshold in the dark matter halo mass of a galaxy below which we find all of our high diffuse H I fractions. Our dark matter halo mass threshold lies around $\sim 10^{11.1} M_{\odot}$. This tells us that we can expect a galaxy with a dark matter halo mass above this threshold to contain no more than about 25% diffuse gas.

- 7. We demonstrate that galaxies with high diffuse HI fractions all have rotation velocities below about 80 km s⁻¹. We suggest this as a regime in which galaxies become dominated by their diffuse gas.
- 8. We use the HI mass of the disks of each galaxy, along with their SFRs, to find the depletion timescales of each galaxy. These depletion times have a large spread, but only four galaxies have depletion times below a Hubble time. Most galaxies in our sample currently have enough H I to continue to fuel star formation for well over a Hubble time, where the median time is 27 Gyr.

The high-resolution MHONGOOSE survey with MeerKAT will provide additional insight into the origins of low column density gas in the CGM of these galaxies. Galaxies with diffuse fractions supporting cold-mode accretion models in our sample will be better understood with higher-resolution data. With these single-dish counterpart data to the MeerKAT interferometer data, we will have a complete census of the H I in each of these galaxies at all angular scales.

A.E.S. is supported by an NSF Astronomy and Astrophysics Postdoctoral Fellowship under award AST-1903834. D.J.P. and A.E.S. acknowledge partial support by NSF CAREER grant AST-1149491. This project has received funding from the European Research Council (ERC) under the European Union's Horizon 2020 research and innovation program grant agreement No. 882793, project name MeerGas. This research made use of the NASA/IPAC Extragalactic Database (NED). The Robert C. Byrd Green Bank Telescope is operated by the Green Bank Observatory. The Green Bank Observatory is a facility of the National Science Foundation operated under cooperative agreement by Associated Universities, Inc.

Appendix

Below we present the remainder of the galaxies in our GBT-MHONGOOSE sample, as we did in Figure 4. Top left: total integrated HI profile measured used to measure the total integrated HI mass. Top right: cumulative HI mass. The total HI mass in the moment 0 map is plotted by the fraction of gas in column density bins and compared to the GBT beam model, scaled to the peak column density. Bottom left: azimuthally averaged $N_{\rm HI}$. Column density is averaged over annuli extending radially from the center of the galaxy and compared to the GBT beam model. The black dashed line characterizes the 1σ noise in each annulus, and the blue dotteddashed line represents the 5σ noise in each annulus. Bottom right: cumulative flux. Fluxes in each of those annuli are summed to obtain a measure of the total flux out to the edge of each map.

ORCID iDs

Amy Sardone https://orcid.org/0000-0002-5783-145X N. M. Pingel https://orcid.org/0000-0001-9504-7386 A. Sorgho https://orcid.org/0000-0002-5233-8260 Claude Carignan https://orcid.org/0000-0001-9089-6151 W. J. G. de Blok https://orcid.org/0000-0001-8957-4518

References

```
Bigiel, F., Leroy, A., Walter, F., et al. 2010, AJ, 140, 1194
Birnboim, Y., & Dekel, A. 2003, MNRAS, 345, 349
Bland-Hawthorn, J., Maloney, P. R., Stephens, A., Zovaro, A., & Popping, A.
  2017, ApJ, 849, 51
Bochkarev, N. G., & Siuniaev, R. A. 1977, SvA, 21, 542
Bond, J. R., Kofman, L., & Pogosyan, D. 1996, Natur, 380, 603
Boothroyd, A. I., Blagrave, K., Lockman, F. J., et al. 2011, A&A, 536, A81
Broeils, A. H., & Rhee, M.-H. 1997, A&A, 324, 877
Carignan, C. 2016, in ASP Conf. Ser., 502, Frontiers in Radio Astronomy and
  FAST Early Sciences Symposium 2015, ed. L. Qain & D. Li (San
  Francisco, CA: ASP), 55, arXiv:1510.03462
Das, S., Sardone, A., Leroy, A. K., et al. 2020, ApJ, 898, 15
de Blok, W. J. G., Adams, E. A. K., Amram, P., et al. 2016, in Proc. MeerKAT
  Science: On the Pathway to the SKA (Trieste: SISSA)
de Blok, W. J. G., Athanassoula, E., Bosma, A., et al. 2020, A&A, 643, A147
de Vaucouleurs, G., de Vaucouleurs, A., Corwin, H. G. J., et al. 1991, Third
   Reference Catalogue of Bright Galaxies (New York: Springer)
Di Teodoro, E. M., & Fraternali, F. 2014, A&A, 567, A68
Haynes, M. P., Giovanelli, R., Martin, A. M., et al. 2011, AJ, 142, 170
Heald, G., de Blok, W. J. G., Lucero, D., et al. 2016, MNRAS, 462, 1238
Heald, G., Józsa, G., Serra, P., et al. 2011, A&A, 526, A118
Ianjamasimanana, R., Walter, F., de Blok, W. J. G., Heald, G. H., & Brinks, E.
   2018, AJ, 155, 233
Kannappan, S. J., Stark, D. V., Eckert, K. D., et al. 2013, ApJ, 777, 42
Katz, N., Keres, D., Dave, R., & Weinberg, D. H. 2003, in The IGM/Galaxy
  Connection. Astrophysics and Space Science Library, ed. J. L. Rosenberg &
  M. E. Putman (Dordrecht: Springer), 185
Kereš, D., Katz, N., Fardal, M., Davé, R., & Weinberg, D. H. 2009, MNRAS,
Kereš, D., Katz, N., Weinberg, D. H., & Davé, R. 2005, MNRAS, 363, 2
Koribalski, B. S., Staveley-Smith, L., Kilborn, V. A., et al. 2004, AJ, 128, 16
Krumholz, M. R., & Dekel, A. 2012, ApJ, 753, 16
Leroy, A. K., Sandstrom, K. M., Lang, D., et al. 2019, ApJS, 244, 24
Madau, P., & Dickinson, M. 2014, ARA&A, 52, 415
Maloney, P. 1993, ApJ, 414, 41
Marasco, A., Fraternali, F., Heald, G., et al. 2019, A&A, 631, A50
Martin, C. L., Shapley, A. E., Coil, A. L., et al. 2012, ApJ, 760, 127
Meurer, G. R., Hanish, D. J., Ferguson, H. C., et al. 2006, ApJS, 165, 307
Moster, B. P., Somerville, R. S., Maulbetsch, C., et al. 2010, ApJ, 710, 903
Pingel, N. M., Pisano, D. J., Heald, G., et al. 2018, ApJ, 865, 36
Rhee, J., Lah, P., Briggs, F. H., et al. 2018, MNRAS, 473, 1879
Roychowdhury, S., Chengalur, J. N., Kaisin, S. S., & Karachentsev, I. D. 2014,
   MNRAS, 445, 1392
Rubin, K. H. R., Weiner, B. J., Koo, D. C., et al. 2010, ApJ, 719, 1503
Sorgho, A., Carignan, C., Pisano, D. J., et al. 2019, MNRAS, 482, 1248
Tully, R. B. 1988, Nearby Galaxies Catalog (Cambridge: Cambridge Univ.
  Press)
```

Turner, J. L., Beck, S. C., Benford, D. J., et al. 2015, Natur, 519, 331

Walter, F., Brinks, E., de Blok, W. J. G., et al. 2008, AJ, 136, 2563